RESEARCH ARTICLE | MARCH 10 2026

Mid-fidelity numerical investigation of the interactional aerodynamics mechanisms in an electrical vertical take-off and landing lift + cruise aircraft

L. Abergo ; M. Malavolti; A. Guardone ; A. Zanotti

Physics of Fluids 38, 036113 (2026)
https://doi.org/10.1063/5.0316657

Physics of Fluids ARTICLE pubs.aip.org/aip/pof

Mid-fidelity numerical investigation of the interactional aerodynamics mechanisms in an electrical vertical take-off and landing lift + cruise aircraft

Cite as: Phys. Fluids **38**, 036113 (2026); doi: 10.1063/5.0316657
Submitted: 14 December 2025 · Accepted: 22 February 2026 ·
Published Online: 10 March 2026

L. Abergo,[a] M. Malavolti, A. Guardone, and A. Zanotti

AFFILIATIONS

Politecnico di Milano, Dipartimento di Scienze e Tecnologie Aerospaziali, via La Masa 34, 20156 Milan, Italy

[a]Author to whom correspondence should be addressed: luca.abergo@polimi.it

ABSTRACT

This paper presents a comprehensive investigation into the aerodynamic interaction mechanisms occurring in a Lift + Cruise electric vertical takeoff and landing aircraft aimed to establish comprehensive knowledge of the flow physics related to an open-geometry reference aircraft and guide the preliminary design of novel Urban Air Mobility vehicle concepts. With this aim, a mid-fidelity aerodynamic solver was employed to evaluate the performance of the isolated rotor and subsequently used to capture the complex interactions between the propulsion system and the airframe at the full-vehicle level. Two Lift + Cruise concepts, equipped with four and eight propellers arranged in three different layouts, were investigated and compared in terms of both performance and flow fields for both hover and climb flight conditions. The study reveals that vertical rotor staggering, specifically with front and rear rotor disks, respectively, below and above the wing, significantly enhances thrust in both hover and climb flight conditions, leveraging beneficial wing-wake interactions. While mid-fidelity tools like DUST effectively capture these complex aerodynamic trends, the eight-rotor configuration shows higher interference levels due to fuselage proximity. Ultimately, these performance gains come with a trade-off of increased flow unsteadiness, which poses potential structural and acoustic challenges for Lift + Cruise aircraft design.

I. INTRODUCTION

The design and development of electric Vertical Take-Off and Landing (eVTOL) aircraft represent a key task for the future of Urban Air Mobility (UAM),[1] since faster point-to-point transportation and less congested cities are expected in relation to population growth. These aircraft exploit multiple rotors/propellers powered by electric-battery technology, enabling vertical takeoff and landing in order to reduce the dependence on traditional infrastructure (such as runways) and to be environmentally friendly. Many different eVTOL architectures have been conceptualized depending on different specific mission profiles, though all the designs have common features and challenges to overcome. Three concepts of eVTOL aircraft have been developed in recent years,[2] as depicted in Fig. 1. Multi-copter, wingless solutions are concepts similar to classical helicopters or drones and are characterized by no thrusters for cruise; they are used only for lift. They exhibit almost the same limitations as classical helicopters in terms of maximum speed achievable in cruise. The vectored-thrust concept shares the main architectural features of tiltrotors and tiltwings that use their thrusters for both lift and cruise. They are suited for higher range and higher speed missions, but they require a more complex design due to the necessity to tilt their propellers during the hover-to-cruise transition maneuver. The Lift + Cruise configuration features completely independent thrusters for cruise and for lift without any thrust vectoring, which allows the aircraft to takeoff and land vertically, similarly to a helicopter, and to achieve high speed in the cruise phase like a traditional aircraft, thanks to the use of classical lifting surfaces. The Lift+Cruise eVTOL configuration represents a quite appreciable compromise in terms of performance for medium-range missions and architectural degree of complication.

The main challenge related to all these concepts concerns the use of multi-propellers and/or Distributed Electric Propulsion (DEP). In particular, an essential aspect for these vehicles' design is an accurate evaluation of the interactional aerodynamic effects between the propellers, as well as between the propellers, wing, and airframe during the

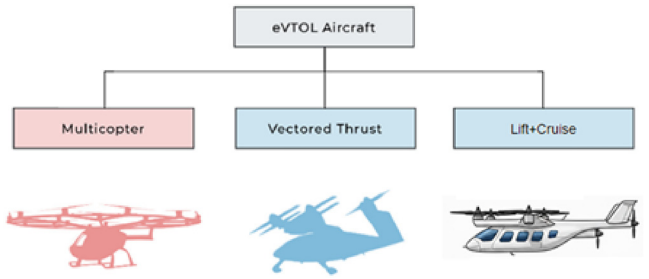

FIG. 1. eVTOL concepts.

different phases that characterize their flight envelope. These interactions significantly influence thrust efficiency, stability, and noise profiles, this latter particularly critical related to the peculiar environment of eVTOLs flight mission, i.e., urban overcrowded areas.

The effects of basic interactions characterizing eVTOL aircraft architectures, i.e., rotor–rotor and rotor–wing, are strictly related to the mutual distance between multiple rotors and lifting surfaces. In particular, rotor-to-rotor interactions vary based on the geometric arrangement and flight phase (hover, transition, or cruise). For tandem rotor configurations in cruise (or airplane mode), the front propeller's slipstream directly impacts the rear propeller, causing the rear propeller to experience significant thrust losses that increase by decreasing the longitudinal distances between the disk planes (Refs. 3–5). The degree of disk overlap is also a critical driver of interference, providing the highest detrimental effects on rear rotor performance for coaxial-like conditions in both hover and cruise flight conditions.[3,6,7] In side-by-side layouts, interaction effects are generally less severe than in tandem setups. Studies show very slight performance losses on the order of few percentages with respect to single rotor case obtained at the lowest lateral distances between adjacent rotor blades.[3,8,9] In addition, rotor–rotor interactions were recently investigated with application to complete multi-rotor aircraft configurations as quad-copters. In particular, the recent work by Kostek *et al.*[10] investigated the effects of vertical and horizontal rotor spacing on aerodynamic efficiency of different quad-copter layouts, particularly focusing attention on the variation of the performance on front and rear rotors.

Concerning rotor–wing interaction effects in DEP systems, recent studies have highlighted their leverage on aero-propulsive benefits for the aircraft system. Sinnige *et al.*[11] conducted a comprehensive comparative study between wingtip and inboard propeller configurations, accounting for both directions of rotation. Specifically, an inboard-up rotation regime was found to benefit the wing's lift coefficient. In contrast, interaction with the propeller slipstream in an outboard-up rotation regime caused a lift penalty compared to the prop-off condition. For a similar layout, Zanotti *et al.*[12] also investigated the sensitivity to longitudinal positioning of the propeller disk with respect to the wing founding that while the wing's performance is relatively insensitive to small changes in this offset, the propeller efficiency itself is significantly affected by the proximity to the wing. Moreover, these experimental data showed that a propeller mounted on the wing exhibits an increased thrust coefficient that is highly dependent on the advance ratio and the local flow field induced by the wing. In a broader design space, Cole *et al.*[13] numerically assessed the influence of propeller location, diameter, and rotation direction. The authors noted that the performance benefits expected from inboard-up propellers are not universal; rather, they are strictly dependent on the specific propeller-wing design and the interplay between these parameters. Notably, the required propeller power showed a correlation with vertical positioning due to the reduction of induced drag within the slipstream. Furthermore, Schollenberger *et al.*[14] investigated the influence of rotational speed, blade count, and pitch angle. Their findings suggested that slower-rotating propellers achieve higher drag reduction, while increasing the number of blades or the pitch angle enhances overall aerodynamic efficiency.

The aim of the present work is to enhance knowledge with respect to basic mechanisms by providing insight into the complex interactional aerodynamic features occurring for a complete Lift + Cruise eVTOL configuration. Due to the recent conceptualization of this eVTOL configuration, a limited number of works employing numerical and experimental approaches to study the main aerodynamic features related to this concept are present in the literature. Among experimental works, Bacchini *et al.*[15] performed wind tunnel tests aimed to quantify the drag penalty of high-lift propellers and their impact on the performance of a Lift + Cruise eVTOL aircraft, while including potential benefits from retracting the propellers during cruise. Westcott *et al.*[16] performed experiments in an anechoic wind tunnel over a wing with vertical lift propellers arranged in a Lift+Cruise layout, simulating the transition from hover to cruise flight conditions.

Despite the complexity and effort related to the realization of an experimental campaign over a Lift + Cruise model, the numerical approach was more often used to investigate the complex interaction phenomena related to such aircraft configurations. As an example of numerical studies, Marepally *et al.*[17] investigated the aerodynamic behavior of slowed-lift rotors at high advance ratios and fully stopped rotors in a representative Lift + Cruise eVTOL configuration using high-fidelity Computational Fluid Dynamics (CFD) simulations. Moreover, Liu *et al.*[18] performed a high-fidelity multidisciplinary analysis for the National Aeronautics and Space Administration (NASA) Lift + Cruise eVTOL Urban Air Mobility concept aircraft[2] by coupling aeromechanics simulations to an unsteady Reynolds-Averaged Navier–Stokes solver based on unstructured, overset grid systems. Although the usage of high-fidelity CFD simulations represents an effective tool for accurately studying complex interaction phenomena, this approach still requires demanding computational effort to be employed in a preliminary design phase of a complex eVTOL aircraft like the Lift + Cruise concept.

To overcome this limitation, mid-fidelity numerical methods have been developed in order to enable faster simulations over a wide design space and to account for the complexity of the interactional flow field.[19] In detail, vortex-lattice and lifting-line theories combined with a Vortex Particle Method (VPM) to model the wakes represent the most promising approaches, providing a quite good compromise between accuracy and computational time with respect to high-fidelity simulations.

Among the recent mid-fidelity aerodynamic solvers, the open-source code DUST[20] was developed by Politecnico di Milano. The DUST code's capabilities were assessed and fully validated against experimental and high-fidelity CFD solutions for several interactional problems, from basic propeller–propeller[5,21] and propeller–wing configurations[22,23] to full eVTOL concepts. In particular, DUST was

employed in the aerodynamic analysis of the vectored-thrust concept vehicle Vahana developed by Airbus,[24] showing a strong correlation between mid-fidelity predictions, flight test data, and high-fidelity CFD results. More recently, DUST was used to investigate the NASA quad-rotor concept vehicle,[25] showing the capability to identify the main interactional aerodynamic mechanisms exposed by this configuration in both hover and cruise flight conditions, as well as their effects on the aerodynamic performance of the front and rear rotors.

This work is, therefore, aimed to close the loop by investigating the third family of eVTOL concept, i.e., the Lift + Cruise, with DUST. In particular, thanks to the low computational effort required to obtain DUST solutions for a complete eVTOL aircraft, the novel aspect of this work is the possibility to perform a comparative study of the interactional aerodynamic mechanisms occurring on two Lift + Cruise eVTOL configurations with open geometry equipped with four and eight rotors, respectively, each characterized by propellers arranged in three positions with respect to the wing. Mid-fidelity simulation results enabled a direct comparison of the flow fields and aerodynamic performance of the different layouts, thus supporting insight regarding the most promising configuration, particularly for hover and climb flight conditions. The present work has been developed according to the framework of DICUAM2026 (Delft International Conference on Urban Air Mobility), which consists in a collaboration among universities and research institutes all over the world aimed at defining knowledge regarding the design of UAM open-source common models.[26]

This paper is organized as follows. Section II analyzes the numerical setup and the geometry definition inside DUST framework. Section III discusses the comparison of the simulations results for the different investigated configurations providing insight for the thrust capabilities and the flow field. Conclusions are drawn in Sec. IV.

II. NUMERICAL MODEL

A. DUST solver

DUST is an open-source, MIT-licensed mid-fidelity aerodynamic solver developed at Politecnico di Milano. It features a coupled formulation integrating distinct aerodynamic models for solid bodies, specifically thick-surface panels, thin vortex-lattice elements, and lifting-line elements. Wake dynamics are described via a Vortex Particle Method (VPM),[27,28] which furnishes a stable, grid-free Lagrangian representation of the free-vorticity flow field, particularly advantageous for simulating configurations with intense aerodynamic interactions (e.g., rotary-wing applications). VPM differs from classical CFD approach by shifting from an Eulerian (fixed grid) to a Lagrangian (moving particle) framework. In particular, VPM eliminates the need for a stationary numerical volumetric grid by solving the velocity-vorticity formulation of the Navier–Stokes equations in a Lagrangian frame. In this approach, the fluid's state is discretized into discrete elements (particles) transporting vorticity by decomposing the velocity field into its potential and rotational constituents, and the governing equations are satisfied by evolving these particles' positions and strengths in physical space. Mathematically, the "domain-free" nature arises because the velocity field is obtained through the Biot–Savart Law, which acts as a fundamental solution to the Poisson equation for velocity, as will be described in detail in the following. This allows the velocity at any point to be calculated as an integral—or a summation over discrete particles—of the vorticity distribution, removing the requirement for artificial boundary conditions at the edges of a truncated computational box.

In this setup, a lifting body sheds a trailing wake from its trailing edge, initially modeled as a series of vortex ring panels. After each temporal integration step, these panels are advected, and a new row is generated. To enhance numerical stability in capturing wake dynamics, these panels can subsequently be converted into vortex particles.

The governing equations implemented in DUST are founded on the assumption of incompressible flow and the application of Stokes' hypothesis to the Newtonian constitutive relation, resulting in the following Navier–Stokes formulation:

$$\nabla \cdot \mathbf{u} = 0, \tag{1}$$

$$\frac{\partial \mathbf{u}}{\partial t} + \mathbf{u} \cdot \nabla \mathbf{u} = -\frac{1}{\rho}\nabla p + \nu \nabla^2 \mathbf{u}. \tag{2}$$

Applying the Helmholtz decomposition theorem then yields the velocity field as the sum of an irrotational vector field $\mathbf{u}_\phi$ and a solenoidal vector field $\mathbf{u}_\psi$,

$$\mathbf{u}_\phi = \nabla \phi, \tag{3}$$

$$\mathbf{u}_\psi = \nabla \psi, \tag{4}$$

where $\mathbf{u}_\phi$ is the potential velocity, $\mathbf{u}_\psi$ is the rotational field, ϕ is the scalar potential, and ψ is the vector potential. As a consequence of their definitions, applying the divergence and curl operators to the decomposed velocity field yields the Laplace equation and the Poisson equation as follows:

$$\Delta \phi = 0, \tag{5}$$

$$-\Delta \psi = \boldsymbol{\omega}, \tag{6}$$

where $\boldsymbol{\omega}$ is the vorticity vector field and, under the incompressible fluid hypothesis, its form reads as

$$\frac{\partial \boldsymbol{\omega}}{\partial t} + \mathbf{u} \cdot \nabla \boldsymbol{\omega} = \boldsymbol{\omega} \cdot \nabla \mathbf{u} + \nu \nabla^2 \boldsymbol{\omega}. \tag{7}$$

In a Vortex Particle Method (VPM), the vorticity field is approximated by a Lagrangian discrete scheme and discretized via vortex particles with intensity $\alpha(t)$ at position $\mathbf{r}(t)$. These Lagrangian elements are called vortex particles, and the vorticity field approximation is

$$\boldsymbol{\omega}(\mathbf{r}, t) = \sum_{i=1}^{N_p} \boldsymbol{\alpha}_i(t) \xi(\mathbf{r} - \mathbf{r}_i(t)), \tag{8}$$

where $\xi(\mathbf{r})$ is a cutoff function of the vorticity induced by the vortex particles. The equations governing the evolution of the position and intensity of a generic particle i can be derived by substituting Eq. (8) into Eq. (7), yielding

$$\frac{d\mathbf{r}}{dt} = \mathbf{u}(\mathbf{r}_i(t), t), \tag{9}$$

$$\frac{d\boldsymbol{\alpha}_i}{dt} = \nabla \mathbf{u}(\mathbf{r}_i(t), t)\boldsymbol{\alpha}_i + \nu'' \Delta \boldsymbol{\alpha}_i''. \tag{10}$$

The first expression describes the convection of particles by the local velocity $\mathbf{u}(\mathbf{r}_i)$, whereas the second governs the temporal evolution of their intensity $\boldsymbol{\alpha}_i$, as dictated by diffusion and vortex stretching-tilting. Collectively, Eq. (9) constitutes the governing equations for this problem.

The rotational velocity component, $\mathbf{u}_\psi(\mathbf{r}, t)$, arises from both the vortex particles and the line vortices associated with the vortex panels. By applying Green's function method to Eqs. (9) and (6), this velocity field can be derived from the vorticity distribution as follows:

$$\mathbf{u}_\psi(\mathbf{r}_i, t) = \sum_{i=1}^{N_p} \mathbf{K}_\xi \times \boldsymbol{\alpha}_{i_p}. \tag{11}$$

In this formulation, $\mathbf{K}(\mathbf{r}, \mathbf{r}_0)$ denotes the consistent velocity kernel, derived from the Biot–Savart kernel through the integration of a cutoff function $\xi(r)$. The primary role of this function is to regularize the expression, removing the singularity that occurs in $\mathbf{K}(\mathbf{r}, \mathbf{r}_0)$ as r approaches r_0. This specific equation accounts for the velocity field generated by the vortex particles.

A Lagrangian grid-free strategy bypasses the necessity for generating a volume mesh of the ambient flow. The vortex particle method, in particular, is highly effective at capturing wake interactions from lifting surfaces, a common challenge in rotary-wing vehicle simulations. By enforcing vorticity conservation directly through the governing equations, this method significantly curtails numerical dissipation. In contrast, standard mesh-based CFD approaches require extensive grid refinement to resolve wakes from lifting bodies accurately, especially during the complex aerodynamic interactions typical of multi-rotor systems.

To maintain computational efficiency for extensive VPM simulations, a Cartesian Fast Multipole Method (FMM)[29,30] is employed to accelerate particle-interaction calculations. The evaluation of aerodynamic loads depends on the specific element: lifting-line elements utilize tabulated sectional coefficients, while surface panel loads are derived from the unsteady Bernoulli's theorem, including the flow's vorticity component. The exhaustive mathematical framework of the solver is detailed in Tugnoli *et al.*[20,31]

B. Lift + Cruise DUST model

The layout of the Lift + Cruise aircraft was built in the frame of this project to define a reference open-geometry configuration for common investigation of such eVTOL concepts. The aircraft employed rotors exploiting a two-bladed propeller geometry extensively tested by Deutsches Zentrum für Luft- und Raumfahrt (DLR). The propeller geometry, described in Yin *et al.*,[32] was properly scaled to fit the dimensions required to reproduce a full-scale eVTOL aircraft. It is noted that the aerodynamic model adopted in this study is based on a linear vortex lattice formulation coupled with a vortex particle method, which assumes inviscid flow conditions. As a result, Reynolds number effects are not explicitly accounted for, and the scaling is intended to preserve geometric similarity rather than Reynolds number similarity. A simple fuselage geometry was purposely designed by the DICUAM2026 consortium, while the wing exploits the geometry of the NASA Lift + Cruise eVTOL aircraft described in Leonard and Litherland[33] and Silva *et al.*[34] The wing and fuselage are depicted in Fig. 2, also showing their main dimensions. The wing incidence angle with respect to the fuselage is 2°. Two aircraft configurations were investigated in the present simulations, i.e., a four-rotor version and an eight-rotor version. A fixed rotor diameter of $R = 2$ m and $R = 1.5$ m was considered, respectively, for the four-rotor and eight-rotor aircrafts. For both configurations, three versions were investigated, characterized by different positioning of the rotors with respect to the wing, i.e., the baseline, having the propeller disks aligned with the wing chord, the rotors-up, with propeller disks positioned upward with respect to the wing, and the rotors-downup, with front and rear rotor disks, respectively, below and above the wing. The different aircraft version layouts are shown in Fig. 3, where the indicated dimensions are included in Tables I and II. The reference system used for the activity is depicted in Figs. 2 and 3. The nacelles and the pylons of the propellers were not considered in the numerical models. The complete geometry of the aircraft components used to build the numerical models investigated in the present work will be released at the end of the dissemination activities planned at DICUAM26 Conference https://www.dicuam2026.org on the website of the project UAM Open Source Model.[26]

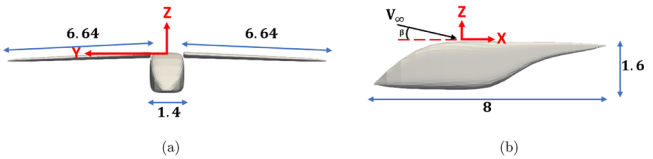

FIG. 2. DUST model—Wing and fuselage main dimensions [m].

The rotor blades have been modeled as vortex lattice elements, while the wing and the fuselage as surface panels. Each blade of the rotors was modeled by a total number of 400 vortex lattice elements, using a spanwise discretization of 40 elements and a chord-wise discretization of 10 elements. A half-cosine refinement was applied to the elements in the chord-wise direction, similarly in the spanwise direction a refinement is applied at the blade tip, as shown in the mesh layout depicted in Fig. 4(a). The wing were modeled using a total number of 500 surface elements, using a spanwise discretization of 25 panels and a chord-wise discretization of 10 panels for each of the half-wing, while the fuselage was discretized with a total number of 852 surface panels [see Fig. 4(b)]. The numbers of elements used to build the numerical models for DUST simulations are summarized in Table III.

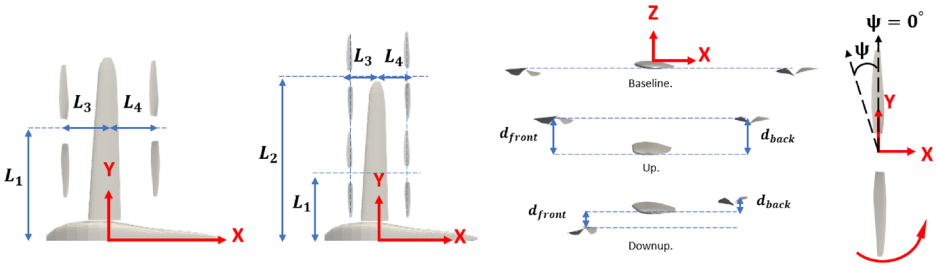

FIG. 3. DUST model—Definition of the four- and eight-rotor Lift + Cruise aircraft configurations.

TABLE I. Four-rotors model—Geometrical parameters [m].

	L_1	L_3	L_4	d_{front}	d_{back}
Baseline	4	−4	4	0	0
Up	4	−2.5	2.5	0.7	0.7
Downup	4	−2	2	−0.35	0.35

TABLE II. Eight-rotors model—Geometrical parameters [m].

	L_1	L_2	L_3	L_4	d_{front}	d_{back}
Baseline	2.7	6.85	−3	3	0	0
Up	2.7	6.85	−2	2	0.7	0.7
Downup	2.7	6.85	−1.5	1.5	−0.35	0.35

The number of elements selected for each rotor blade was suggested by the results of a sensitivity study performed against experimental results available from Abergo *et al.*[35] for the single rotor in hover-flight condition. On the other hand, the selection of the number and the discretization of the surface panels used to model the wing and the fuselage was based on best practices achieved to model similar aircraft configurations.[24,36]

In addition a combined spatial and temporal discretization sensitivity study is performed on the complete vehicle. Simulations are carried out in hover using the "4-rotor-up" configuration, while the discretization of the wing and fuselage is kept unchanged. Two more grid resolutions are considered, with 200 collocation points for the coarse grid and 600 for the denser grid. On the reference (medium) grid, both a larger and a smaller azimuthal time step are additionally tested.

The results, summarized in Table IV, show that—consistently with the findings obtained for the isolated rotor in hover—a time step of 3° in azimuth on the medium grid provides a good compromise between accuracy and computational cost. This configuration is, therefore, adopted for all subsequent simulations, which are run for a total of seven complete rotor revolutions. The models' wake is simulated by VPM using a maximum of 1×10^6 particles. Specifically, DUST mid-fidelity simulations of each of the three different Lift + Cruise layouts previously described were performed in hover and climb-flight conditions. The cruise-flight condition, characterized by stopped lifting propellers for Lift + Cruise aircraft configurations, was not investigated in the present activity, thus leading to the choice not to consider the pusher propeller in the numerical models. For both hover and climb conditions, rotors' rotational speed was set in order to reproduce the same $M_{tip} = 0.3$ for the four-rotor and eight-rotor models, corresponding, respectively, to 492 *RPM* and to 656 *RPM*. This Mach tip has been proved to provide a good compromise between

TABLE III. Summary of aircraft elements used to model the Lift + Cruise aircraft in DUST.

	Spanwise	Chordwise	Tot.
Rotor blade	40	10	400
Left wing	25	10	250
Right wing	25	10	250
Fuselage	...	...	852

TABLE IV. Effect of grid resolution and time step size on vertical force statistics for the four-rotor-up configuration in hover. Reported values are computed over the last three rotor revolutions and correspond to the total contribution of all propellers.

Grid	Time step	F_z (N).	Variation (%)	Std Dev. F_z (N)
Coarse	3 deg	18052	−3.18	2.3
Denser	3 deg	18808	+0.88	3.5
Medium	1 deg	18661	+0.09	15.4
Medium	3 deg	18644	+0.00	2.5
Medium	5 deg	18611	−0.18	9.8

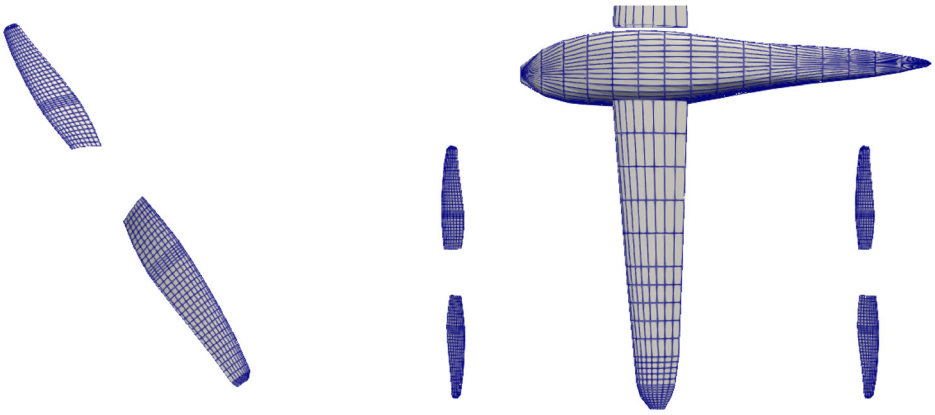

(a)Rotor blades (b)Wing and Fuselage.

FIG. 4. DUST model surface mesh.

aerodynamic efficiency and tonal noise emission for a multi-propeller configuration.[8] For climb simulations, the aircraft velocity was equal to 26.7 m/s associated with a climb angle of 20° with respect to the horizontal direction [see Fig. 2(b)]. The flight conditions were chosen inside the DICUAM consortium and used by all the partners to design different type of eVTOL.

III. RESULTS AND DISCUSSION

Simulation results are now discussed separately for hover and climb flight conditions. Due to the fact that the investigated Lift + Cruise aircraft geometries were novel and purposely developed by the consortium for the present activity, a validation of the numerical models built in this work against high-fidelity CFD results or experiments cannot be performed. Nevertheless, the robustness of the present models, built using the best practices acquired by the DUST development research group, is supported by the several past activities from the same group finalized to a thorough validation of DUST models for complete advanced rotorcraft configurations, such as tiltrotors and eVTOLs, showing accurate agreement with respect to experiments and high-fidelity CFD simulations, as well as flight test data.[24,25,36]

In this section, simulation results obtained over the different investigated aircraft layouts are compared in terms of the produced thrust (force normal to rotor disk) and torque (referred to the rotor hub center) values (averaged over the last computed revolution) and flow field topology. Specifically, Q-criterion three-dimensional visualizations, vorticity field slices, and load distribution over the rotor disk are employed to comprehensively highlight the interactional effects occurring between propellers and due to the different investigated installations with respect to the wing and fuselage.

A. Hover flight condition

As a first step of the aerodynamic performance analysis, the average integral thrust and torque generated by the installed rotors for the different investigated aircraft layouts are compared with the performance of the rotors considered as a single. With this aim, Tables V and VI show the percentage variation of the installed rotors' thrust (T_{inst}) and torque (Q_{inst}) with respect to the values generated by the single rotor multiplied by the number of rotors considered for investigated layouts (T_{rot} or Q_{rot}), i.e., four or eight. Figure 5 highlights the thrust fluctuations around the mean value, allowing a comparison among the different configurations, showing that the down–up configuration exhibits the largest fluctuations that are related to higher interactional mechanisms occurring between rotors wake and fuselage/wing components, as will be discussed later on in the analysis of the flow fields.

TABLE V. Comparison of the variations of the average integral thrust generated by the installed rotors for the different investigated aircraft layouts in hover condition.

$(T_{inst} - T_{rot})/T_{rot}[\%]$	Four rotors	Eight rotors
Baseline	−0.95	−0.48
Up	−0.89	−1.23
Downup	2.8	0.16

TABLE VI. Comparison of the variations of the average integral torque generated by the installed rotors for the different investigated aircraft layouts in hover condition.

$(Q_{inst} - Q_{rot})/Q_{rot}[\%]$	Four rotors	Eight rotors
Baseline	0.26	−1.81
Up	−1.83	−2.69
Downup	−0.08	−3.84

In hover conditions, a slight loss of the global thrust is observed for the installed rotors for both the baseline and rotors-up configurations, regardless of the number of rotors. On the other hand, a slight increase in the generated thrust can be appreciated for the rotors-downup configuration, indicating a favorable interactional effect between the rotor wakes and the airframe in this arrangement that is more evident for the four-rotor configuration, while it is quite negligible for the eight-rotor configuration. As a result of the same interactional mechanisms, reduction of rotor torque is also generally observed for the investigated configuration, except for the baseline and downup cases with four rotors showing a quite negligible variation of torque with respect to the case that considers rotors as single. This favorable effect on torque is particularly occurring for both the rotors-up configurations and for the downup layout with eight rotors, thus confirming the promising performance improvement that could be obtained for this latter configuration.

In order to investigate the correlation between performance variation and flow physics, in the following, the topology of the flow fields

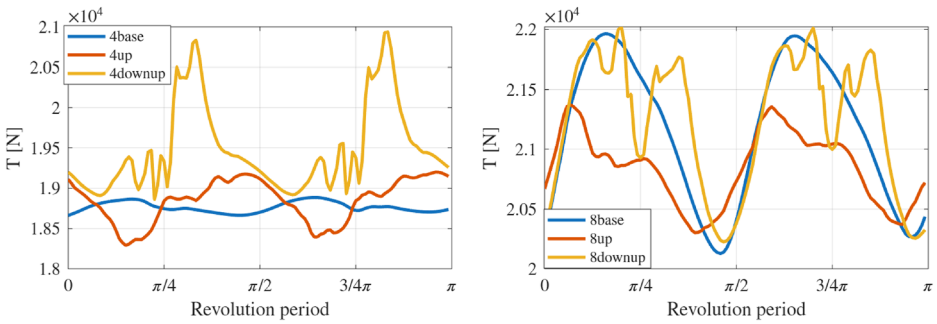

(a)4-rotors (b)8-rotors

FIG. 5. Hover flight, comparison of the thrust time history, obtained by summing the contributions of all rotors and averaging over the last three simulated revolutions.

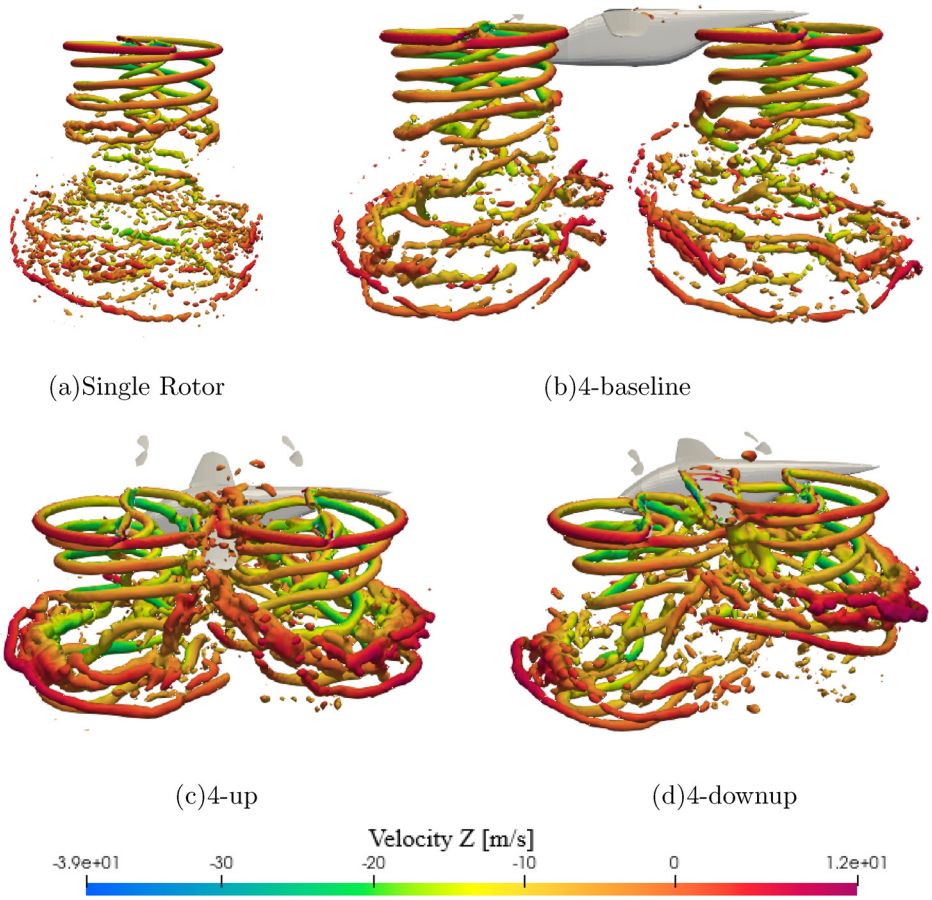

FIG. 6. Hover flight, comparison of the flow fields for the 4-rotors configurations, and Q-criterion three-dimensional surfaces contoured by vertical velocity.

is compared for the different aircraft layouts, including the single rotor configuration. In Fig. 6, the hover case of the four-rotor configuration is investigated by means of a three-dimensional visualization of the Q-criterion colored by the vertical velocity component (V_z), which highlights coherent vortical structures shed by the rotors.

For the single rotor case, the wake is allowed to fully develop and the classical helical tip-vortex system is clearly visible [see Fig. 6(a)]. In contrast, in the four-rotor baseline configuration the rotors are located relatively far from the wing, such that neither rotor-to-rotor nor rotor-to-wing interactions appear to be strongly manifested [see Fig. 6(b)]; effectively, each rotor behaves nearly independently and produces thrust levels comparable to the isolated case.

When more compact or vertically-staggered layouts are considered, however, the rotor–airframe and rotor–rotor interference become significant. In the "4-rotor-up" and "4-rotor-downup" configurations, the previously coherent helical wakes degrade rapidly just below the wing plane, giving rise to increased turbulence and flow unsteadiness [see Figs. 6(c) and 6(d)]. Such breakdown of coherent tip-vortex structures has direct implications for the induced-velocity field at the rotor disks and hence for the effective blade-angle-of-attack and thrust distribution along the blade span, as will be discussed later on.

To support a more quantitative assessment, Fig. 7 shows vorticity magnitude contours extracted on the vertical plane cutting through the hub centers of the front and rear rotors. Figure 7(b) shows that for the baseline case, tip-vortices near the wing have sufficient separation to fully develop and even intensify with respect to the isolated case [see Fig. 7(a)]. Indeed, only slight mixing between the wakes of the front and rear rotors occurs downward of the disk plane for the baseline configuration. On the other hand, for the "4-rotor-up" case, Fig. 7(c) shows that the vortices generated at blade tips remote from the wing are drawn inward and downward, resulting in a coalesced, single, more-intense wake structure beneath the vehicle. This merged wake is especially pronounced in the rear rotor region, thereby dominating the thrust distribution at that disk. Conversely, when the rotor operates in close proximity to the wing (as in the "4-rotor-downup" layout), the tip-vortex immediately impacts the wing after separation and cannot fully develop. The consequence is the formation of a high-vorticity zone on the wing's leading and trailing edges, which perturbs the thrust coefficient of both front and rear rotor disks [clearly evident in Fig. 7(d)]. Such rotor–wing interaction aligns with recent findings in the eVTOL literature, where wake deformation and induced-flow augmentation due to closely spaced rotors or adjacent lifting surfaces lead to thrust losses and altered performance.[5,24,37] For completeness, the vertical velocity contours on an X–Z vertical plane passing through the rotors centerline are reported in Appendix (see Fig. 21).

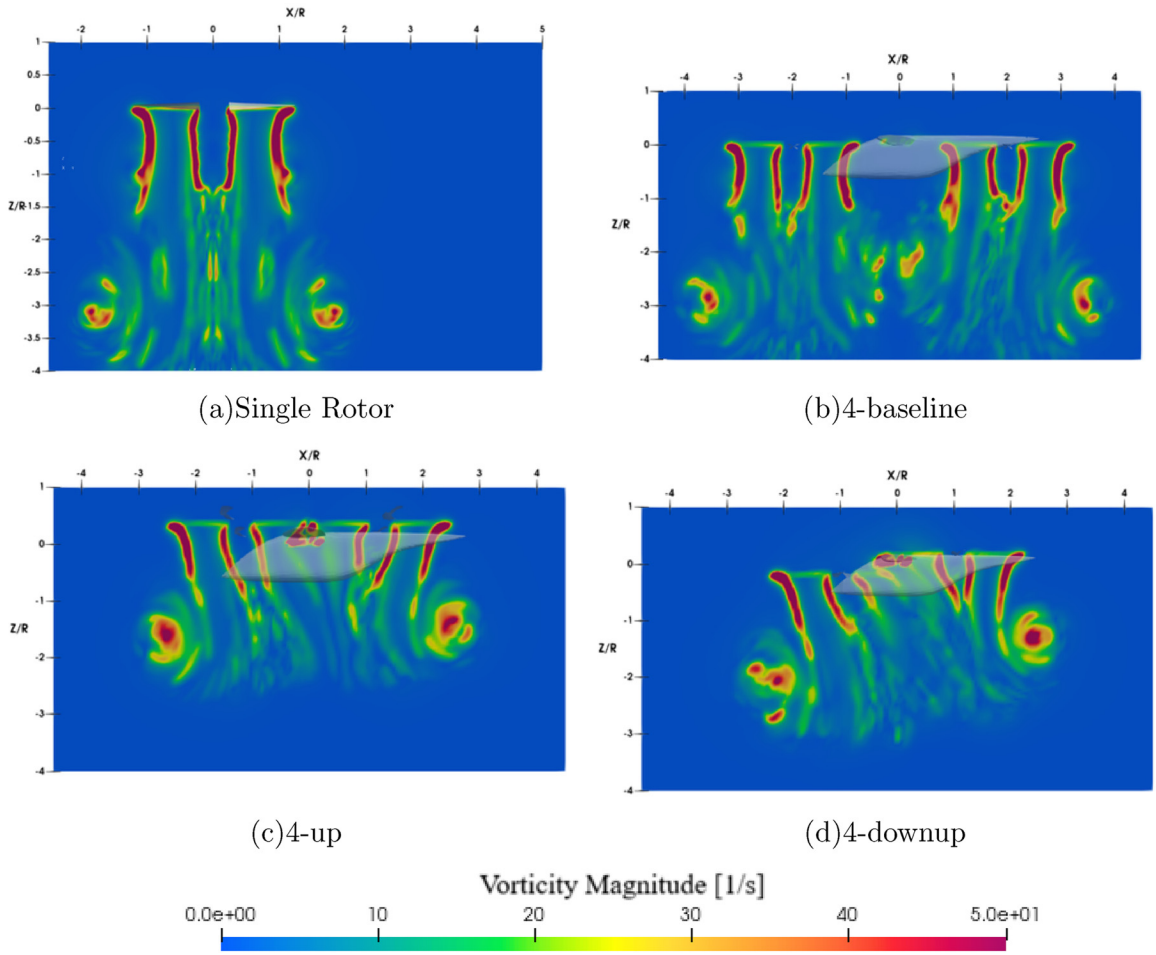

FIG. 7. Hover flight, comparison of the flow fields for the 4-rotors configurations, and vorticity magnitude contours on a $X - Z$ vertical plane passing though the rotors hubs centerline.

A quantitative confirmation of the wake-interaction effects previously discussed is provided by the comparison of the vertical velocity component profiles extracted over a line placed at $z = -1[m]$ passing through the frontal and rear rotor center (see Fig. 8) and through the frontal rotors center (see Fig. 9). In the "4-rotor-baseline" configuration [see Figs. 8(a) and 9(a)], the vertical velocity component distribution remains nearly symmetric with respect to both longitudinal and lateral axis and exhibits full velocity recovery for both the front and rear rotors, comparable to the single rotor case. The influence of the airframe is evident in the positive vertical velocity at the center of the curve. In the "4-rotor-up" layout [see Figs. 8(b) and 9(b)], the vertical velocity profile becomes more perturbed with respect to single rotor case, showing stronger variations immediately downstream of the front rotor and over the fuselage area. The proximity of the rotors to the wing promotes early interaction between the rotor wake and the wing surface, which accelerates the flow locally and alters the induced velocity entering the rear rotor. Compared with the single rotor condition, the vertical velocity beneath the front disk becomes less negative, indicating a reduction of the downwash intensity and partial blockage of the flow due to the wing proximity. This effect reduces the effective inflow uniformity and modifies the local induced velocity distribution at the rear rotor plane. A more complex trend is observed in the "4-rotor-downup" configuration [see Figs. 8(c) and 9(c)]. Here, the front-rotor wake is deflected downward by the wing and impinges directly on the rear-rotor inflow. As a result, the velocity recovery between the two disks nearly disappears, and the magnitude of the downward velocity below the rear rotor increases significantly compared with the single rotor case. On the other hand, the velocity profiles extracted with respect to Y-axis keep a quite symmetrical behavior showing slight differences with respect to the midspan plane of the fuselage due to the fact that the two frontal rotors blades spin with the same sense of rotation.

All the wake interaction phenomena described are reflected in the distribution of the thrust generated by the rotor disks. The evolution of the thrust coefficient along the azimuthal angle ψ during the last computed revolution is analyzed for both the front and rear rotors, and compared with the single rotor case in Fig. 10. The azimuthal angle definition is depicted in Fig. 3.

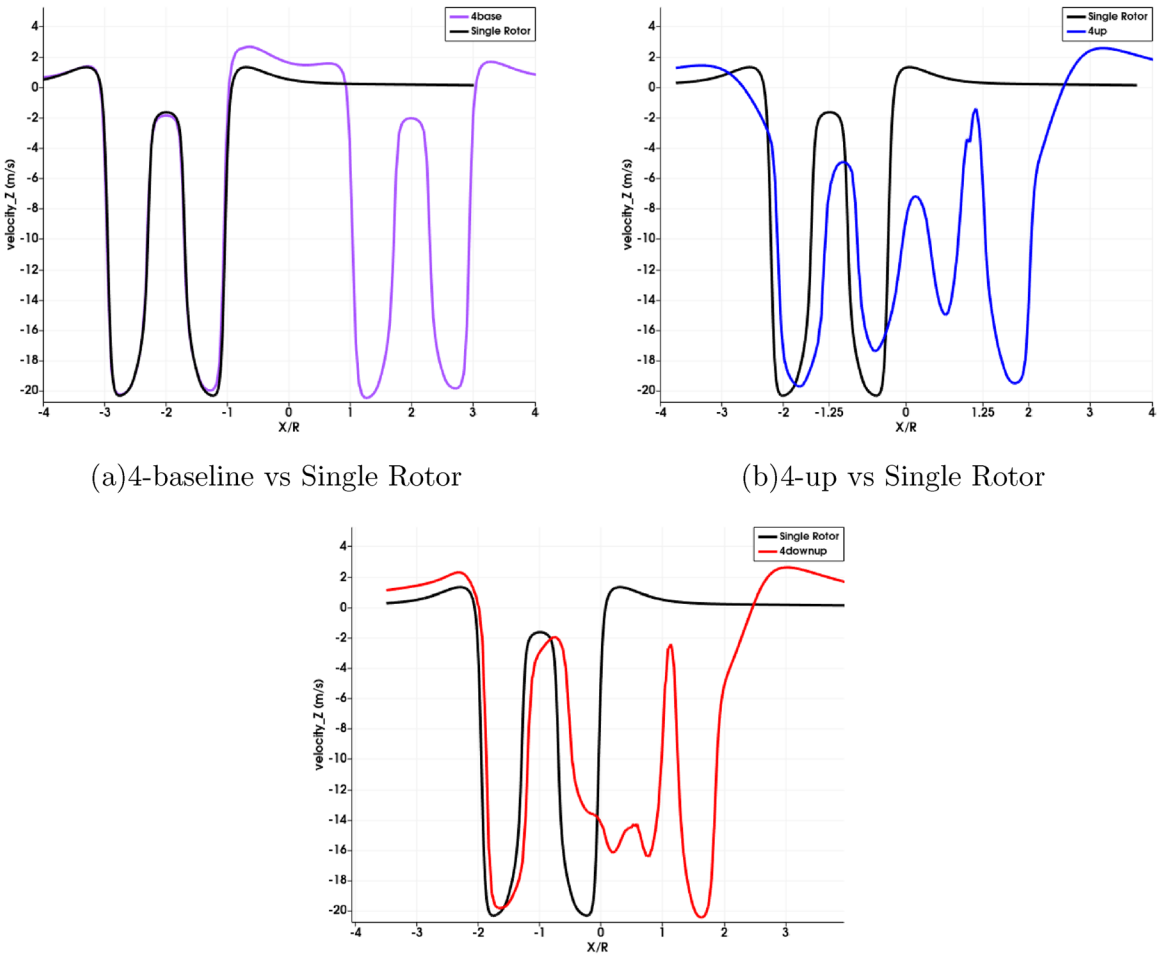

(a)4-baseline vs Single Rotor

(b)4-up vs Single Rotor

(c)4-downup vs Single Rotor

FIG. 8. Comparison of the vertical velocity component profiles extracted over a line placed at $z = -1[m]$ passing through the frontal and rear rotor center, 4-rotors configurations in hover.

Figure 10(a) clearly shows that for the baseline configuration, the C_T distribution generated by the rotors remains nearly symmetric, with overall intensity closely resembling that generated by the single rotor case. Indeed, for the sake of consistency, only the rear rotor distribution is presented in Fig. 10(a), as for the baseline case, front and rear rotors exhibit the same thrust distribution in hover-flight condition due to the fact that their installation does not provide apparent interference with the wing. The behavior of the thrust distribution resembles the mean integral thrust generated, respectively, by the two front and rear rotors shown in Table VII. Indeed, in the baseline configuration, the two front and rear rotors generate almost the same level of integral thrust.

In the 4-rotor-up configuration [see Fig. 10(b)], a noticeable asymmetric behavior appears in the C_T distributions between the front and rear rotor. Indeed, rotor interaction with the wing generates a loss of thrust with respect to the single rotor configuration in the range between $240^\circ < \psi < 300^\circ$ for the front one and between $60^\circ < \psi < 150^\circ$ for the rear rotor, which is also affected by the interaction with the fuselage in the range between $350^\circ < \psi < 60^\circ$. In addition, the rear rotor experiences a thrust rise with respect to the baseline configuration over the remaining disk area, in agreement with the observed local increase in vertical velocity shown in Fig. 8(b), thus reflecting the variation of the rotor induced velocity provided by the interactions with the airframe discussed earlier. Generally, the rear rotor generates an integral thrust value that is higher than the one provided by the front rotor in the same configuration and than the one generated by the same rear rotor in the baseline configuration (see Table VII).

Concerning the 4-rotor-downup layout, this configuration shows the largest interactional effects on rotors thrust generation due to the partial overlap occurring with respect to the wing. In particular, thefront rotor exhibits a larger increase in thrust in the region $0^\circ < \psi < 180^\circ$ with respect to the "4-rotor-up" configuration. Moreover, the rear rotor disk shows strong positive fluctuations in the region of passage of the blades over the wing, i.e., $60^\circ < \psi < 120^\circ$. This latter effect is mainly

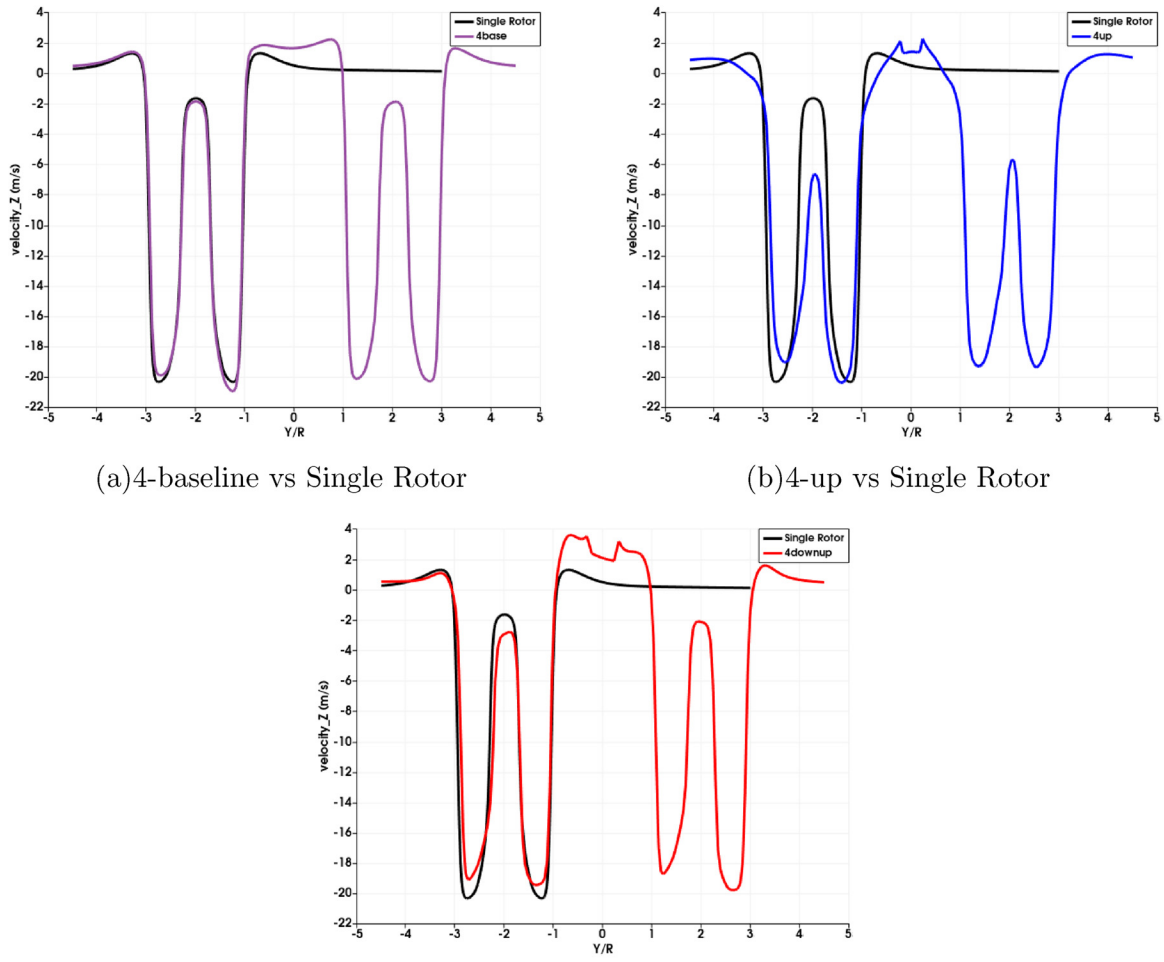

(a)4-baseline vs Single Rotor

(b)4-up vs Single Rotor

(c)4-downup vs Single Rotor

FIG. 9. Comparison of the vertical velocity component profiles extracted over a line placed at $z = -1[m]$ passing through the frontal rotors center, 4-rotors configurations in hover.

responsible for the largest integral thrust generated by the rear rotor in the "4-rotor-downup" configuration (see Table VII), even if associated with loading overshoots that could be detrimental for structural or noise-signature issues. Nevertheless, the largest increase in the integral thrust is also observed for the front rotor, thus confirming the favorable effect in terms of aircraft performance provided by interactional mechanisms occurring between rotors and the airframe for this latter layout.

The focus now shifts to the eight-rotor configurations. Analogously to what has been done for the four-rotor configurations, Fig. 11 compares the three-dimensional flow fields calculated for the different eight-rotor configurations by means of the Q-criterion surfaces contoured by vertical velocity. Moreover, wake interactions can be analyzed more quantitatively by the contours of vorticity magnitude extracted over a vertical plane passing through the rotor's hub centreline, shown in Fig. 12. In addition, for 8-rotor configurations, the vertical velocity contours on the other vertical plane X–Z vertical plane are reported in Appendix but not commented (see Fig. 22).

By analyzing the baseline case, the lateral view of the three-dimensional flow field shows negligible interactions between the front and rear rotors' wakes [see Fig. 11(a)]. This behavior is confirmed by the vorticity magnitude contours extracted over a lateral slice of the domain [see Fig. 12(a)]. On the other hand, the front view representation of the three-dimensional flow field shown in Fig. 11(b) highlights a more pronounced interaction between the side-by-side rotors, as well as between the internal rotors and the fuselage. Generally, wake topology becomes more complex with respect to the corresponding 4-rotor case. Indeed, the frontal slice of the vorticity magnitude field shown in Fig. 12(b) indicates that the tip vortices issued by the side-by-side rotors tend to merge in the region between adjacent disks, thus suggesting the onset of a strong wake interactional mechanism.

Both the 8-rotor-up and 8-rotor-downup layouts exhibit a markedly more complex behavior of the flow field, related to the

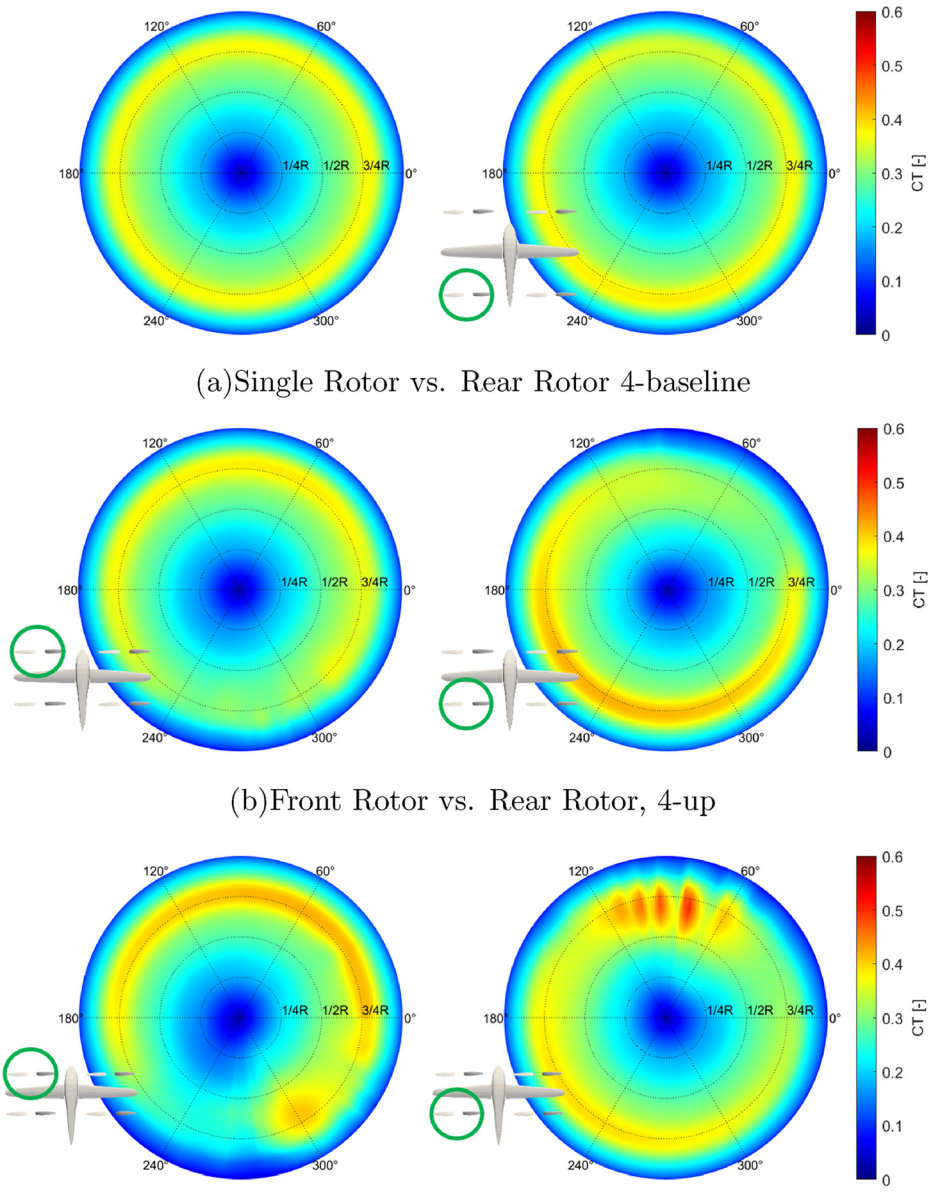

(a)Single Rotor vs. Rear Rotor 4-baseline

(b)Front Rotor vs. Rear Rotor, 4-up

(c)Front Rotor vs. Rear Rotor, 4-downup

FIG. 10. Comparison of the thrust coefficient C_T distribution on the rotor disk evaluated during the last computed revolution, 4-rotor configurations in hover.

TABLE VII. Integral mean thrust generated by the front and rear rotors for the 4-rotor configurations in hover and relative percentage variations with respect to baseline configuration.

Configuration	T_{Front} [N]	T_{Rear} [N]	ΔT_{Front} [%]	ΔT_{Rear} [%]
4-base	4703	4696	...	...
4-up	4675	4837	−0.6	3
4-downup	4789	4979	1.8	6

occurrence of a stronger interaction between side-by-side and tandem rotors and between rotors and the airframe, i.e., the wing and fuselage [see Figs. 11(c) and 11(d)]. In both cases, the classical helical structure issued by the rotors fails to fully develop, and the vortices lose coherence when reaching the region close to the wing surface. Thus, also the symmetry of the vorticity field, clearly visible in the baseline configuration, is no longer preserved [see Figs. 12(c) and 12(d)]. Moreover, by comparing the vorticity magnitude fields for the 4-rotor-downup and 8-rotor-downup configurations, a distinctly different pattern in the vortex-core trajectories can be

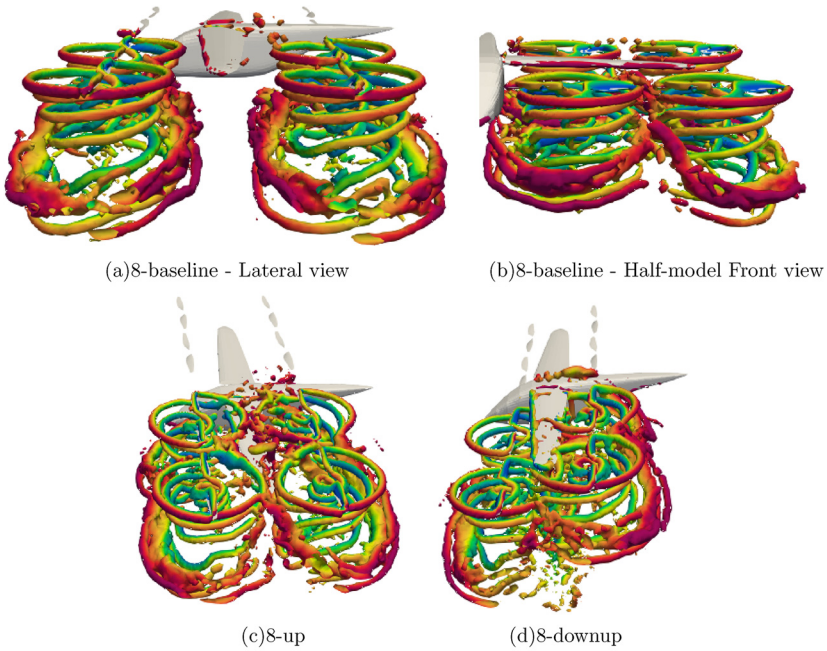

FIG. 11. Hover flight, comparison of the flow fields for the 8-rotors configurations, and Q-criterion three-dimensional surfaces contoured by vertical velocity.

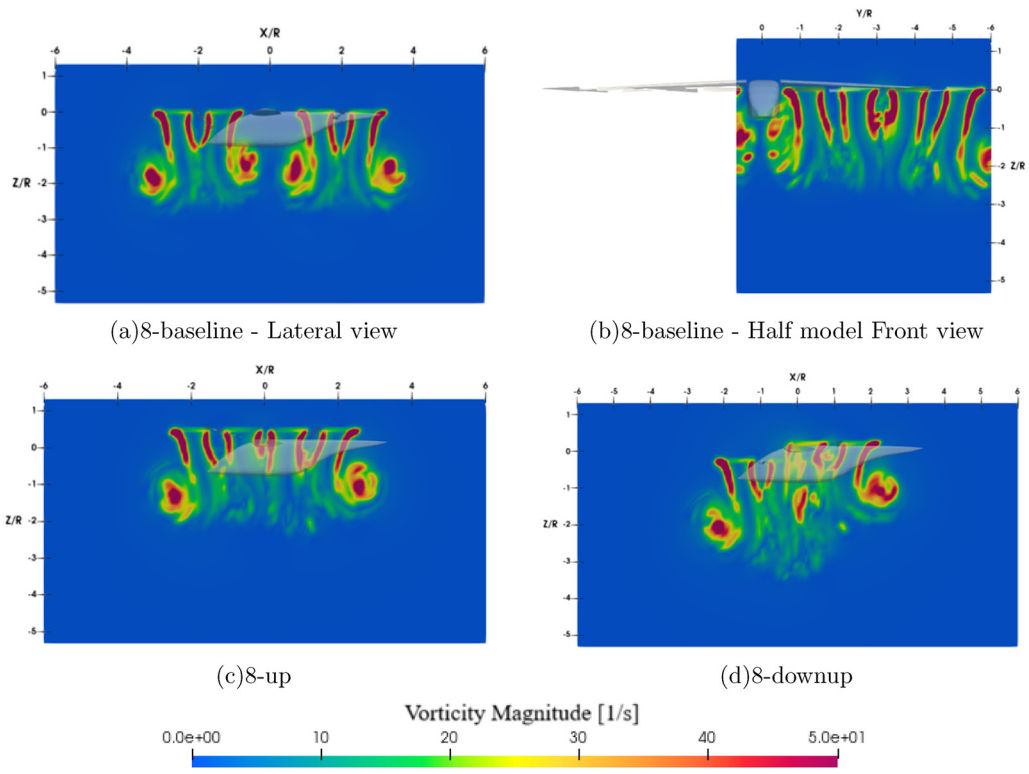

FIG. 12. Hover flight, comparison of the flow fields for the 8-rotors configurations, and vorticity magnitude contours on a vertical plane passing through the rotor hub centerline.

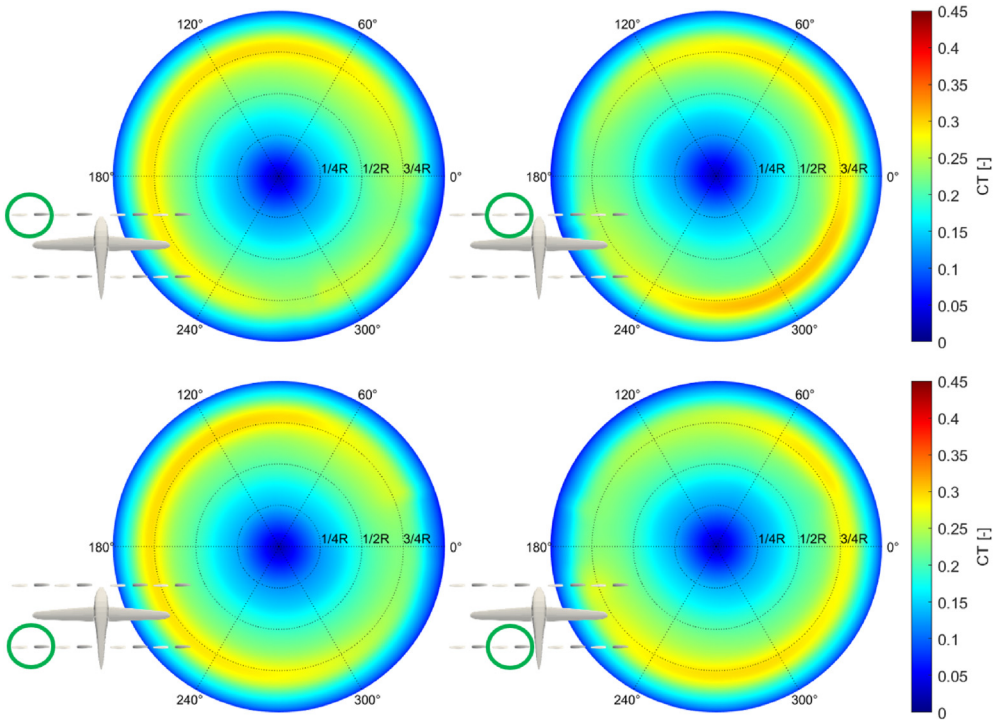

(a)8-baseline

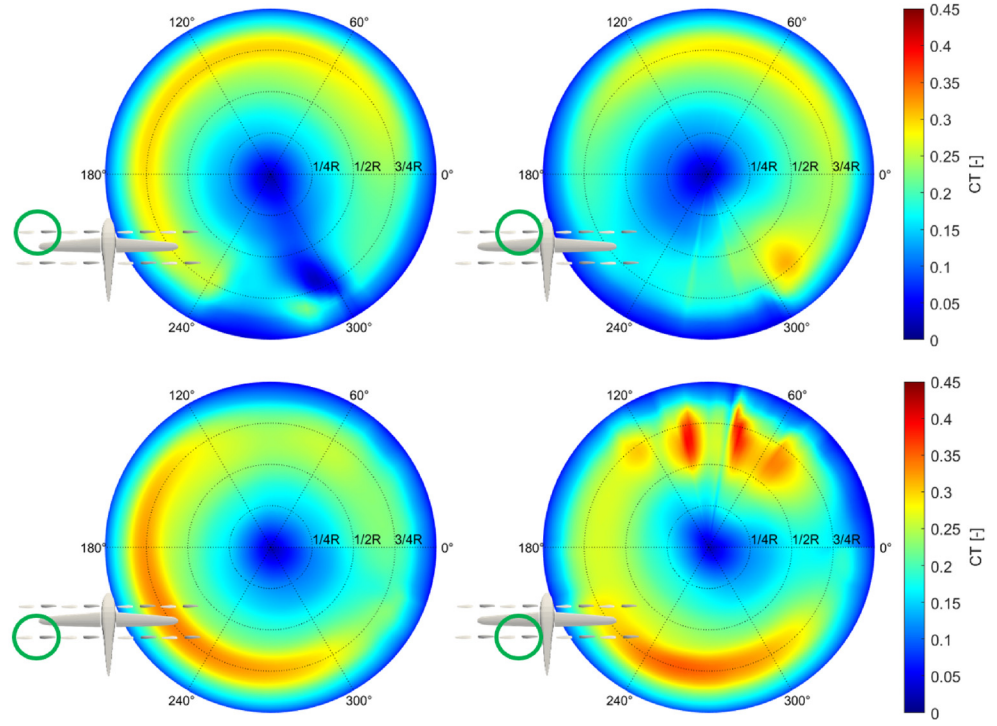

(b)8-downup

FIG. 13. Comparison of the thrust coefficient C_T distribution on the rotor disk evaluated during the last computed revolution, 8-rotor configurations in hover.

TABLE VIII. Integral mean thrust generated by the outer front and rear rotors for the 8-rotors configurations in hover.

OUTER	Front [N]	Rear [N]
8-base	2659	2658
8-downup	2546	2739

TABLE IX. Integral mean thrust generated by the inner front and rear rotors for the 8-rotor configurations in hover.

INNER	Front [N]	Rear [N]
8-base	2637	2623
8-downup	2520	2849

observed. Unlike in the four-rotor vehicle, the vortices issued in the 8-rotor-downup configuration are deflected downward beneath the wing, forming an intense mixing region in the area immediately below it. The remaining portion of the wake retains some organized structure but rolls up closer to the disk plane, producing a vorticity field more similar to that observed in the 8-rotor-up layout. Analogously to the 4-rotors configurations analysis, the distribution of the thrust coefficient C_T over rotor disks is shown in Fig. 13 for the 8-rotors configurations. In particular, the polar representation of the loading is compared for the baseline and downup models showing the greatest interactional effects both for the two front and rear rotors placed on the left side of the aircraft fuselage. For the 8-rotor-baseline configuration, the C_T distributions of the two front and rear adjacent rotors exhibit a symmetrical behavior with respect to the longitudinal separation axis [see Fig. 13(b)]. Indeed, a decrease in the generated thrust can be observed in the azimuthal regions corresponding to the sides of the rotors facing each other, i.e., $300° < \psi < 60°$ and $120° < \psi < 240°$, respectively, for the left and right rotor. A smaller perturbation of the disk loading is also visible in the range between $0° < \psi < 90°$, indicating a minor interaction between the inner front rotor and the fuselage.

In the 8-rotor-downup configuration, the rotor-rotor effects become significantly stronger than in the baseline case, particularly evident for the inner rear rotor showing high positive load fluctuations within the range between $0° < \psi < 120°$ [see Fig. 13(b)]. Notably, for the 8-rotor configurations, the strong positive thrust oscillations observed for the rear rotors also in the 4-rotor-downup layout are confined to the internal rotors only. Moreover, the rear rotors exhibit an increase in generated thrust in the range between $120° < \psi < 300°$ due to a favorable effect provided by the interaction with the wing. Due to the opposite installation of the front rotor with respect to the wing, they exhibit an increase in generated thrust in the range between $240° < \psi < 300°$. Generally, the rear rotors generate a higher contribution to the integral thrust that is most pronounced in the 8-rotor-downup configuration. As reported in Tables VIII and IX, the inner or outer rear rotors produce approximately an increase in 10% of the mean thrust than the front ones, which experience only a mean 4% reduction compared with the values obtained for the 8-rotor-baseline configuration. On the other hand, in the baseline configuration, both the front and back rotors generate a similar amount of integral thrust, confirming the quite lower effect of interactional mechanisms on the aircraft performance.

B. Climb flight condition

As done for the analysis of hover simulations results, a first insight into aerodynamic performance discussion is given for climb flight condition by comparing the average integral thrust generated by the installed rotors with respect to the one provided by the rotors considered as single. Figure 14 highlights the rotors thrust fluctuations around the mean value; in climb conditions, unlike hover, the fluctuations amplitude of the time-variant rotors load is very similar for all configurations, even if for the downup configuration small amplitude fluctuations superimposed the periodic thrust time history behavior are observed due to wake interactions.

The thrust and torque percentage variations shown in Table X highlights that the downup configurations are the most promising in terms of aircraft performance improvement also for climb flight condition. Indeed, for both the 4-rotors and 8-rotors layout, this installation provides the highest increase in the generated thrust and the highest reduction of torque coming from the same interactional mechanisms. This outcome is aligned with the trends of the thrust variations observed in Kostek *et al.*,[10] where vertical staggering between the front and rear rotors of a quad-copter in squared configuration at 10° tilt angle leads to a general increase in the rotors' thrust, particularly the rear ones, while improving the overall efficiency of the system. As a matter of fact,

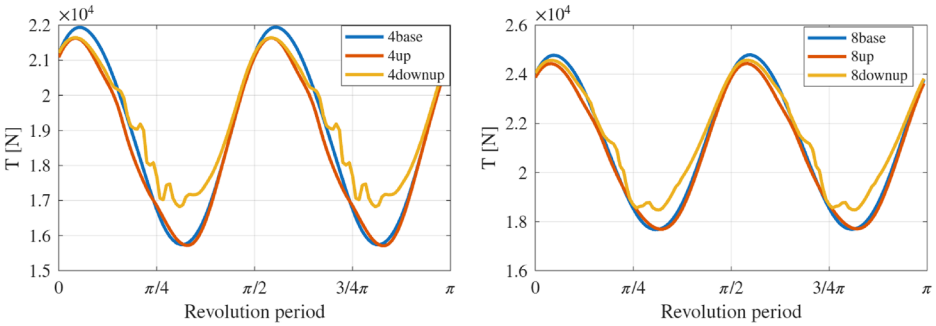

(a)4-rotors (b)8-rotors

FIG. 14. Climb condition, comparison of the thrust time history, obtained by summing the contributions of all rotors and averaging over the last three simulated revolutions.

TABLE X. Comparison of the variations of the average integral thrust and torque generated by the installed rotors for the different investigated aircraft layouts in climb flight condition.

$(T_{inst} - T_{rot})/T_{rot}$ [%]	4-rotors	8-rotors
Base	2.22	1.59
Up	1.05	1.04
Downup	4.20	4.20
$(Q_{inst} - Q_{rot})/Q_{rot}$ [%]	4-rotors	8-rotors
Baseline	−0.23	−0.73
Up	−0.46	−0.84
Downup	−2.01	−2.81

increasing vertical separation between front and rear rotors' disk reduces the aerodynamic interference on rear rotors blades due to the front rotors' wake, as clearly shown later on in the flow field analysis.

Unfortunately, due to the limited number of layouts investigated by DUST simulations, the present analysis cannot distinguish the effects related to the vertical and horizontal staggering of the rotors, as the up and downup configurations considered a combined variation of these two parameters. On the other hand, the horizontal staggering between the front and rear rotors could be considered quite less effective on the overall efficiency of the system, as evidently supported by the results of Kostek *et al.*[10] showing that the variation of the rotors horizontal hub spacing only canceled proximity effects on the front rotors efficiency.

Generally, all the rotors installation layouts investigated in the present work show a slight variation of performance in terms of generated thrust and torque reduction with respect to the rotors considered as single. In particular, the baseline layout performs slightly better than the 4-up configuration in terms of thrust increase, where this latter configuration only shows negligible performance variations with respect to single rotor configuration. In addition, negligible variations in terms of torque reduction are observed for the baseline and rotors-up configurations.

In order to better understand the interactional flow features that influence the rotors performance, three-dimensional visualizations of Q-criterion are used to describe the flow field around the investigated configurations. A first analysis of the flow field is given in Fig. 15 considering the single rotor reproducing the rotational speed and dimensions of the 4-rotors aircraft layout, i.e., 492 *RPM*. As a matter of fact,

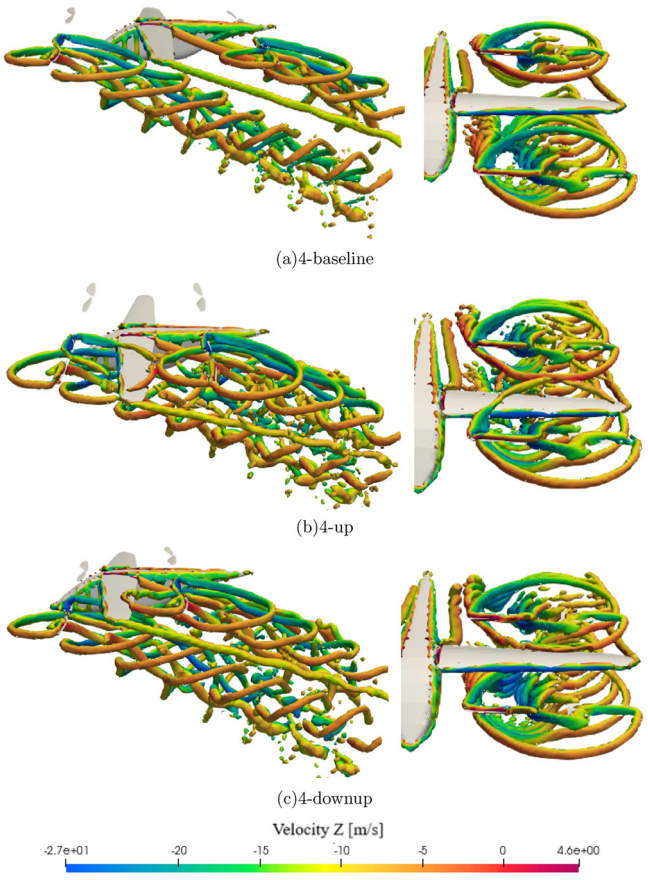

FIG. 16. Climb flight, comparison of the flow fields for the 4-rotors layout, and Q-criterion three-dimensional surfaces contoured by vertical velocity.

in climb flight condition due to the presence of a non-negligible inflow velocity component, the rotor wake is strongly convected downstream and loses coherence much farther from the disk plane with respect to hover. Indeed, as shown in Fig. 15(a), the single rotor case displays a quite coherent helical wake structure convected along the freestream direction.

Nevertheless, the inclined inflow associated with the climb attitude introduces a more complex interaction mechanism between

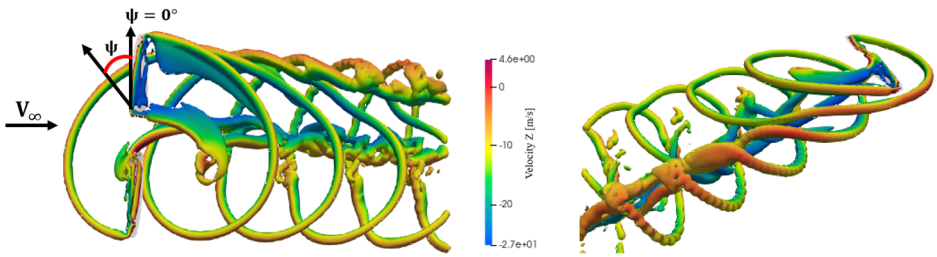

(a)Single Rotor, top view (b)Single Rotor, lateral view

FIG. 15. Climb flight, comparison of the flow fields for the single rotor in the 4-rotors layout, and Q-criterion three-dimensional surfaces contoured by vertical velocity.

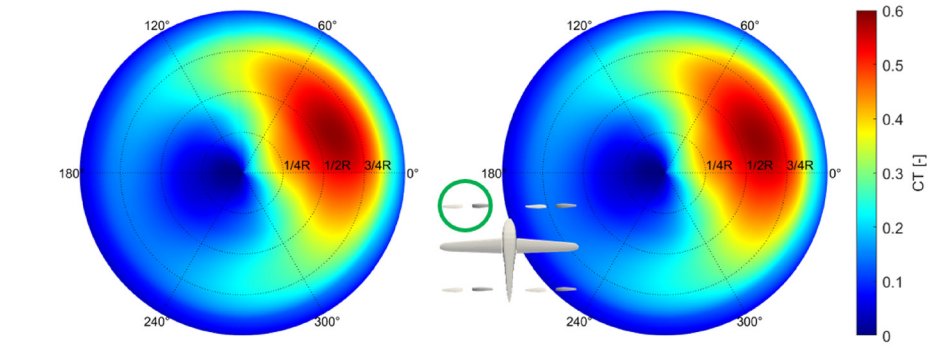

(a) Single Rotor vs. Front Rotor, 4-baseline

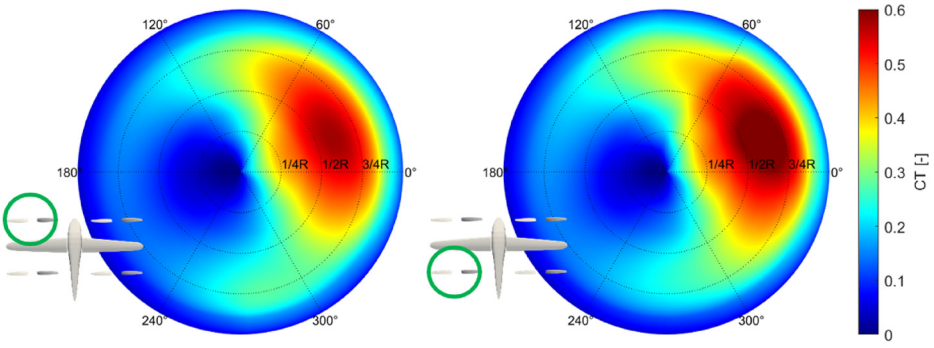

(b) Front Rotor vs. Rear Rotor, 4-up

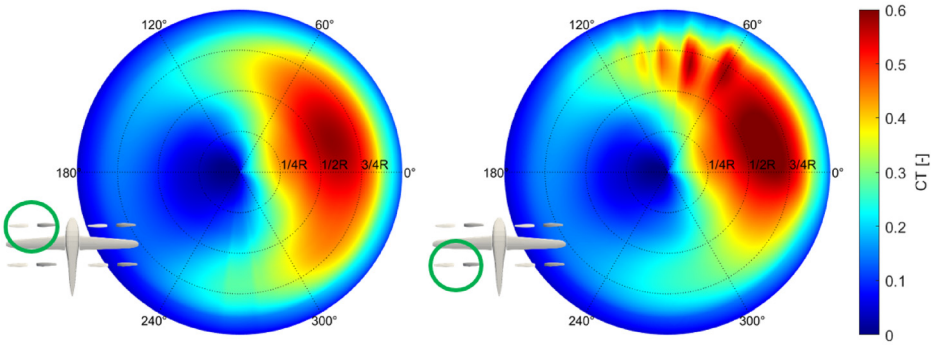

(c) Front Rotor vs. Rear Rotor, 4-downup

FIG. 17. Comparison of the thrust coefficient C_T distribution on the rotor disk evaluated during the last computed revolution, 4-rotor configurations in climb.

blades and their wakes. In particular, a strong blade-vortex interaction occurs through the direct impingement of the tip vortex onto the blade surface. It is worth noting that the tip of the retreating blade encounters the tip vortex shed by the advancing blade at $\psi = 0°$, leading to the merging of the two helical filaments [see Fig. 15(b)]. This impingement event marks the onset of strong unsteady aerodynamic loads, which are characteristic of the climb condition analyzed in this study.

Concerning the complete 4-rotor aircraft layouts, the 4-rotor-baseline case [see Fig. 16(a)] does not show apparent interactions between the rotors' wakes and the airframe, as their helical structures keep their coherence while being convected downstream. On the other hand, evident interactions occur particularly between the front rotor wake and the wing for the 4-rotor-up case [see Fig. 16(b)], also providing an alteration of the wing-tip vortex pattern. Moreover, the helical structures issued by the front and rear rotors touch each other, generating a mixing of the wakes downstream.

The flow visualization for the 4-rotor-downup layout shows a clear interaction of the rear rotor wake with the wing, while less apparent interaction between the front and rear rotor can be observed with

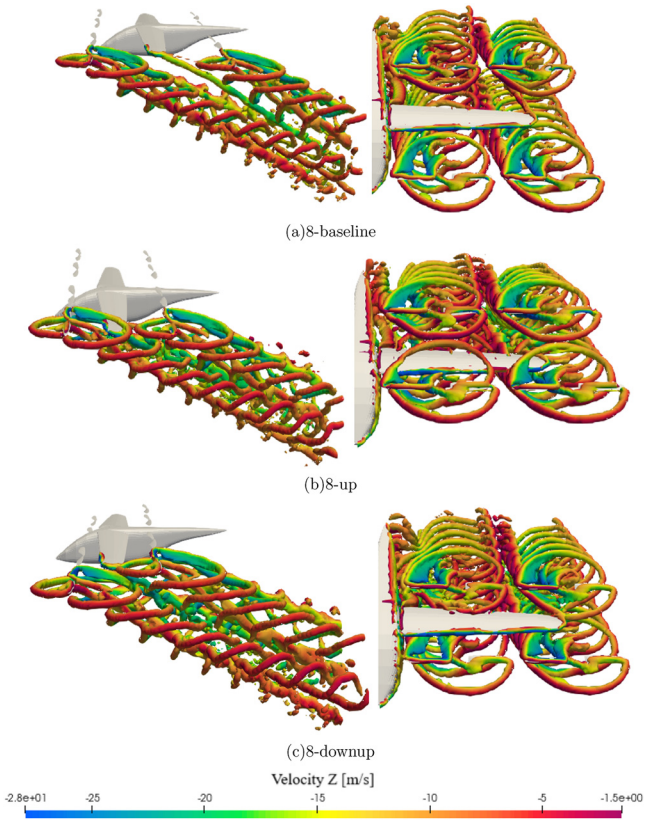

FIG. 18. Climb flight, comparison of the flow fields for the 8-rotors layout, and Q-criterion three-dimensional surfaces contoured by vertical velocity.

respect to the 4-rotor-up case due to the different vertical installation of the rotors [see Fig. 16(c)].

In order to correlate the flow physics phenomena with the rotors' performance, as previously done for the hover simulations analysis, the polar representation of the thrust coefficient C_T distribution computed over the last revolution is shown in Fig. 17 for both the front and rear rotors in the 4-rotor layouts, compared with the single rotor case in climb. All the C_T polar plots evaluated for the different investigated configurations highlight the classical behavior expected for a rotor at incidence, showing higher loading on the advancing side[21] and a certain phase lag[38] correlated with the amount of the tilting angle (i.e., 20°) of the disk with respect to the freestream velocity vector characterizing the climb flight condition. In particular, the comparison between the polar C_T distributions observed for the single rotor and the front rotor in the 4-rotor-baseline layout clearly supports the occurrence of negligible interference effects between rotors and airframe for this installation, even if slightly higher values of C_T can be observed between $0° < \psi < 70°$ in the 4-rotor-baseline case [see Fig. 17(a)].

Concerning the 4-rotor-up layout, even in climb flight, the rear rotor produces a higher thrust with respect to the frontal one, as shown by the more intense loading characterizing the advancing side of the rear rotor disk in the 4-rotor-up configuration [see Fig. 17(b)].

On the other hand, when dealing with the 4-rotor-downup layout, two main features are apparent. The first is related to the wider azimuthal area characterized by higher loading observed for the advancing side of the front rotor with respect to the corresponding rotor in the 4-rotor-up and 4-rotor-baseline case. The second is related to a similar increase in thrust generation occurring on the rear rotor, this time characterized by high fluctuations of the loading due to the interactional effect between the rotor wake and the wing, in particular, in the azimuthal region between $60° < \psi < 100°$ [see Fig. 17(c)].

Analogously to what was observed in hover, flow field analysis for the 8-rotor configurations resembles quite more complicated features. Thus, Q-criterion surface visualizations shown in Fig. 18 are assisted by vorticity contours visualizations over two vertical planes passing through the hubs centerline of the external and internal rotors (see Fig. 19).

As observed for the 4-rotor layout, the 8-rotor-baseline three-dimensional flow visualization does not show apparent interactions between the front and rear rotors' wakes, which naturally evolve downstream [see Fig. 18(a)]. In addition, due to the streamwise velocity component characterizing climb flight, the wakes of the side-by-side rotors also negligibly interact in the baseline configuration. Both these features are supported by the vorticity contours visualizations, highlighting no apparent superpositions of the wakes streamtube edges for both the internal and external rotors [see Figs. 19(a) and 19(b)]. In addition, particularly the slice cutting the internal rotor centerline does not show any impingement of the rotors' wakes with the wing, even if a certain influence on the rear wake behavior could be observed due to the interaction with the fuselage.

The 8-rotor-up layout visualization shows that, since all the rotors are placed over the wing, the wake of the front external rotor impinges partially on the wing tip, while the front internal rotor wake interacts strongly with the wing upper surface [see Fig. 18(b)]. This latter event is apparently observed from the vorticity contours visualizations on the internal rotors slice, showing the generation of a region of intense vorticity in correspondence with the wing leading edge [see Fig. 19(d)].

The 8-rotor-downup layout resembles a wake evolution similar to the baseline case for the external rotors, since both the front and rear external rotors' wakes do not show any strong interactions with the airframe components [see Fig. 18(c)]. On the other hand, as shown by vorticity visualizations in Fig. 19(f), only the rear internal rotors' wake tends to interact with the rear portion of the wing due to their lower relative distance with respect to the 8-rotor-baseline layout. Again, for completeness, the vertical velocity contours on the other plane, namely the X–Z plane passing through the rotors centerline, are reported in Appendix (see Fig. 23). As done for the 4-rotor configurations, the distribution of the thrust coefficient C_T over rotor disks is shown in Fig. 20, particularly comparing the baseline and rotors-downup models only, as they show the greatest differences for the investigated front and rear rotors positioned on the left side of the fuselage.

For the 8-rotor-baseline configuration, the thrust coefficient distributions show a similar behavior for the front rotors and the rear external one, while a slightly higher intensity of the C_T can be observed for the advancing blade of the rear internal rotor between $0° < \psi < 60°$ due to an interaction with the fuselage. Generally,

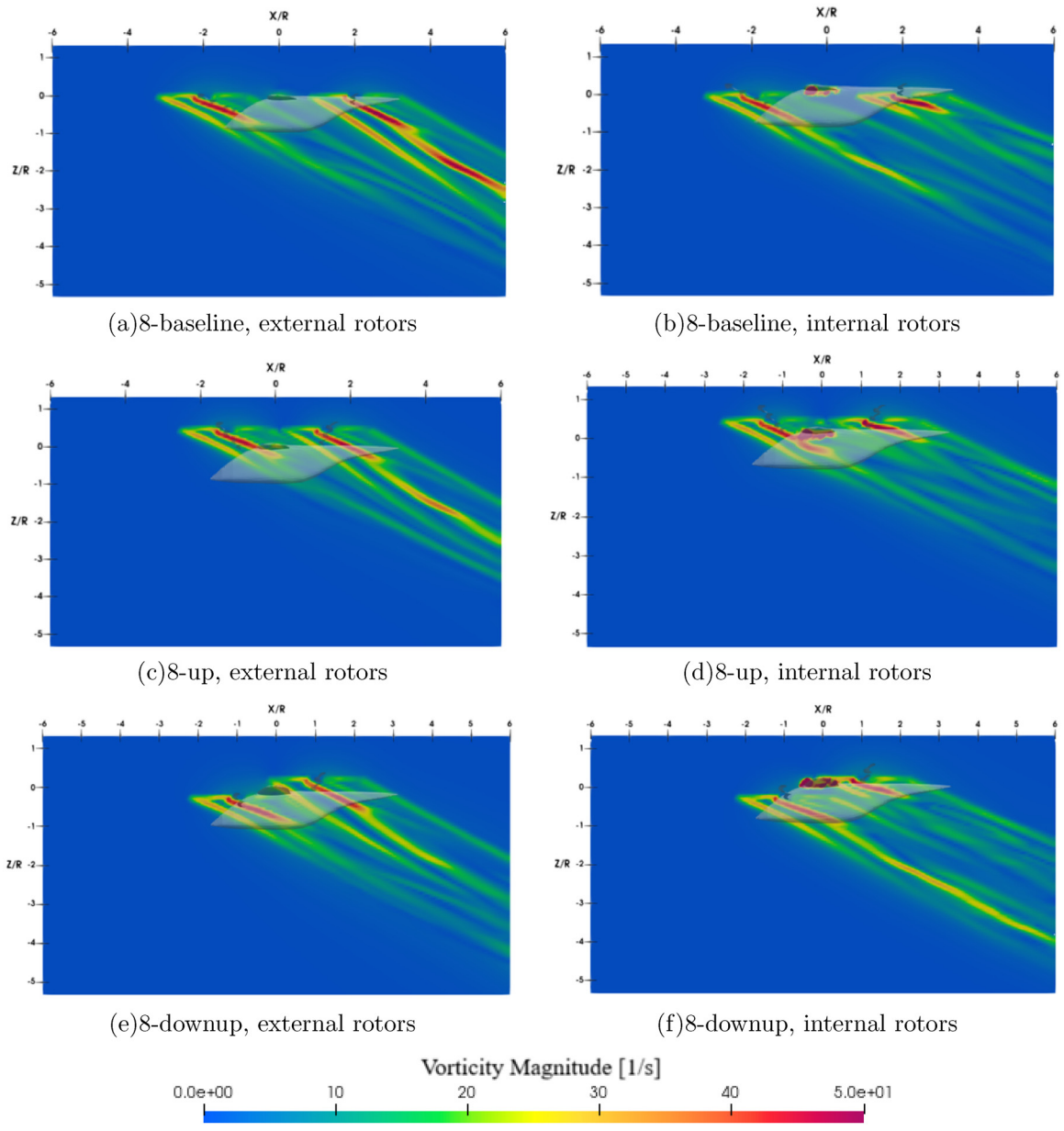

FIG. 19. Climb flight, comparison of the flow fields for the 8-rotors configurations, and vorticity magnitude contours on a $X - Z$ vertical plane passing through the rotors hub centerline.

for the 8-rotor-downup layout, the rear rotors produce a higher level of thrust than the frontal ones, particularly the internal one, which also shows an intense interaction with the wing in the azimuthal range between $60^\circ < \psi < 120^\circ$, characterized by large thrust fluctuations.

IV. CONCLUSIONS

The present work described a comprehensive mid-fidelity numerical investigation of the interactional aerodynamic mechanisms occurring on two Lift + Cruise eVTOL configurations equipped with four and eight rotors. Using the open-source DUST solver, six distinct layouts were simulated in hover and climb to examine how the vertical placement of the rotors with respect to the wing influences wake development, rotor–rotor interference, and rotor–airframe aerodynamic performance. Across all configurations, the simulations demonstrated that the interactional flow field is highly sensitive to the relative distances between rotors and lifting surfaces. In hover, the baseline layouts showed limited aerodynamic interference, with thrust

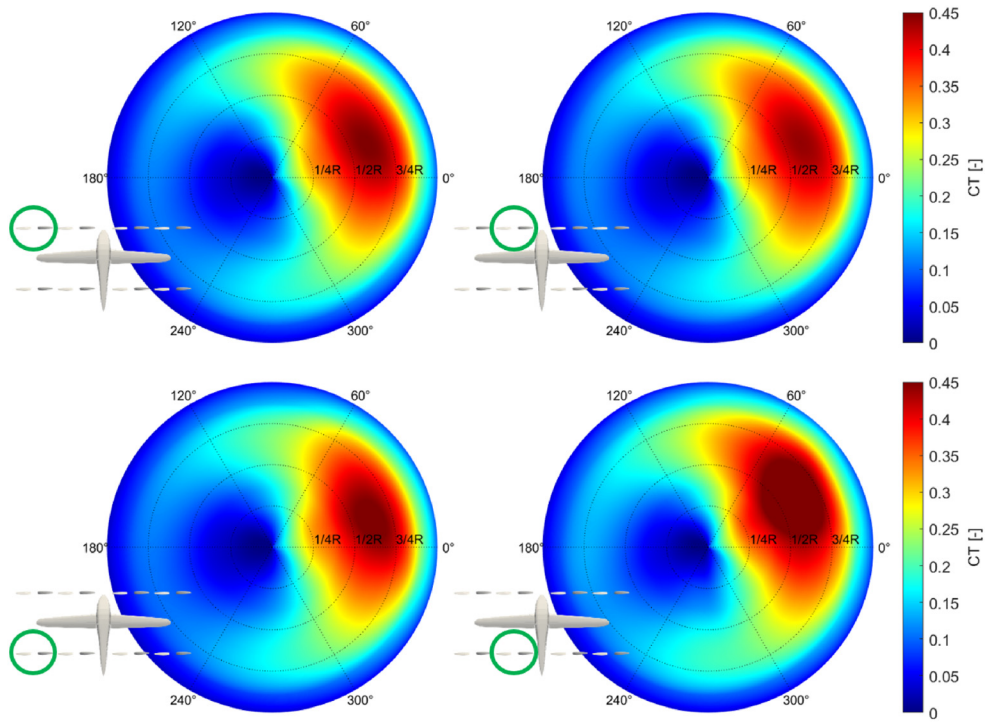

(a)8-baseline

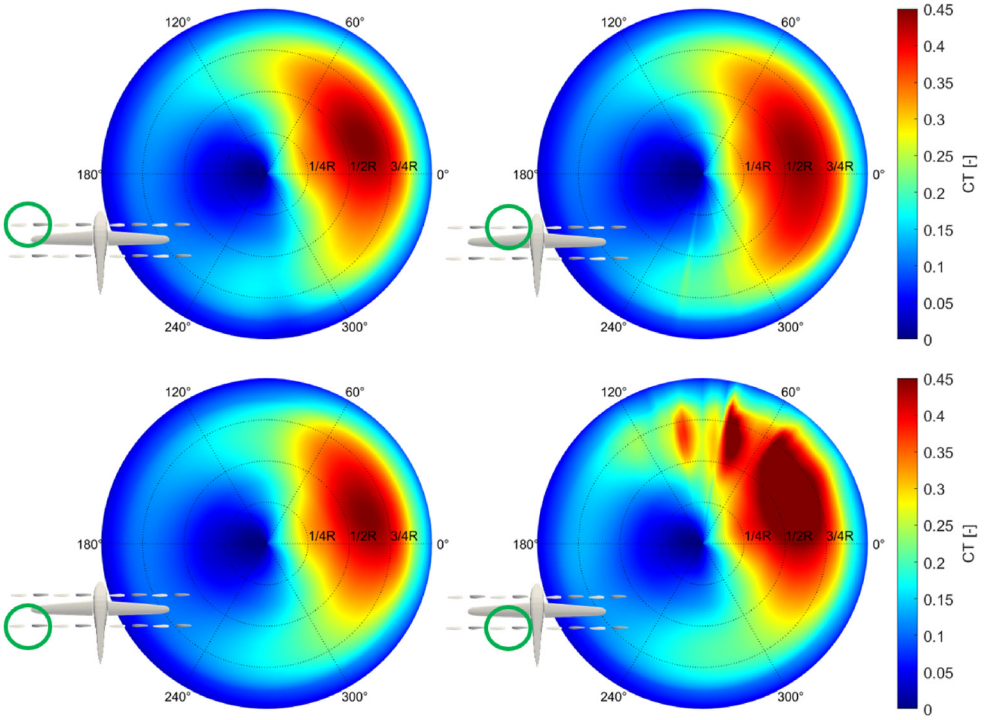

(b)8-downup

FIG. 20. Comparison of the thrust coefficient C_T distribution on the rotor disk evaluated during the last computed revolution, 8-rotor configurations in climb.

levels close to those of the isolated rotors. Conversely, the rotors-up and rotors-downup layouts exhibited strong wake deformation, loss of coherence of the helical structures, and significant perturbations of the induced velocity field. These effects produced minor variations of loads coefficient distributions and asymmetric loading patterns. Among the investigated layouts, only the rotors-downup configuration showed a valuable favorable performance improvements particularly for the four-rotors configuration where an increase in 2.8% of thrust is generated with respect to single rotor case primarily due to the beneficial interaction between the rotor wakes and the wing.

In climb flight, the inflow inclination and increased convective transport of vorticity reduced the near-field wake interference compared with hover, but stronger blade-vortex interactions were observed. Also in this flight condition, minor variations of the performance are observed among installed-rotor configurations, with the rotors-downup layout only delivering a valuable improvement of 4.2% generated thrust for both aircraft sizes. The eight-rotor variants displayed more complex wake behavior, particularly for the inner rotors, where proximity to the fuselage and wing amplified load fluctuations and induced velocity distortions.

Overall, the study confirms that mid-fidelity methods such as DUST can provide valuable insights into the complex aerodynamic flow mechanisms and wake interaction trends governing distributed-propulsion eVTOL aircraft, enabling a fast evaluation of preliminary design-level insights. Indeed, the comparative assessment of the flow features characterizing rotor layouts provided interesting guidelines for the preliminary investigation the interactional mechanisms of novel architectures reproducing the Lift + Cruise concept, widely investigated among the eVTOL community. The results and modeling approach developed in this work contribute to the definition of an open-geometry reference Lift + Cruise aircraft within the DICUAM2026 initiative and support future investigations aimed at optimizing UAM vehicle performance across the flight envelope. Future work could be focused on the use of higher-fidelity CFD simulations to strengthen confidence in the prediction of wake interactions and particularly to provide robustness to rotor loading variations related to the architecture changes investigated in this study to be considered as definitive design advantages for the aircraft.

ACKNOWLEDGMENTS

The present work has been developed according to the framework of *DICUAM*2026.[26]

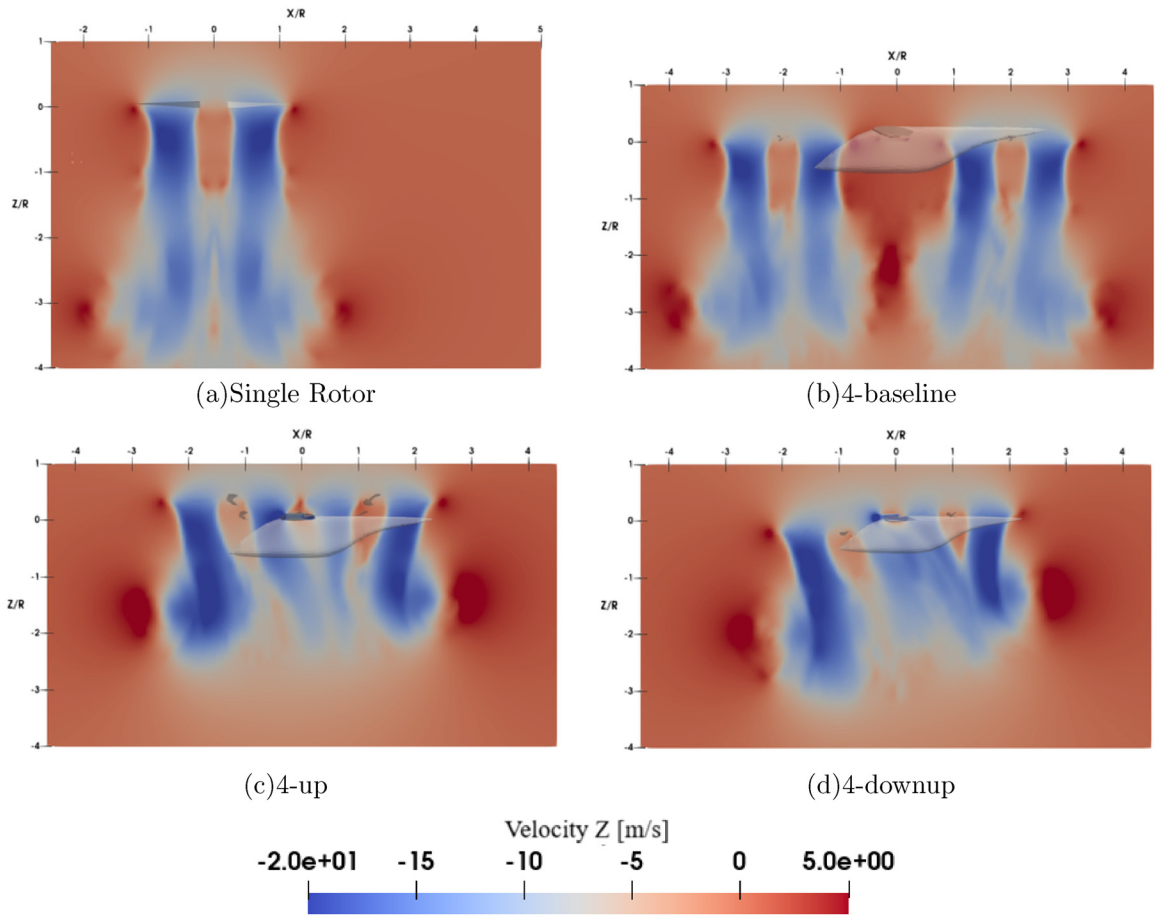

FIG. 21. Hover flight, comparison of the flow fields for the 4-rotors configurations, and vertical velocity contours on a $X - Z$ vertical plane passing though the rotors centerline.

AUTHOR DECLARATIONS

Conflict of Interest

The authors have no conflicts to disclose.

Author Contributions

L. Abergo: Conceptualization (equal); Investigation (equal); Methodology (equal); Writing – original draft (equal). **M. Malavolti:** Investigation (equal); Methodology (equal); Validation (equal); Writing – original draft (equal). **A. Guardone:** Project administration (equal); Supervision (equal); Writing – original draft (equal). **A. Zanotti:** Conceptualization (equal); Project administration (equal); Supervision (equal); Writing – original draft (equal).

DATA AVAILABILITY

The data that support the findings of this study are available from the corresponding author upon reasonable request.

NOMENCLATURE

C_T	thrust coefficient $= T/(\rho\pi R^4 n^2)$ [-]
d	vertical distance of rotors
eVTOL	electrical vertical take-off and landing aircraft
L	lateral distance of rotors
n	rotational speed (rad/s)
Q	rotor torque (N m)
R	rotor radius (m)
RPM	revolution per minute
T	rotor thrust (N)
UAM	urban air mobility
velocity Z	vertical velocity component (m s^{-1})
$x-y-z$	reference system axis
ρ	freestream air density (kg m^{-3})
ψ	blade azimuthal position (deg)

APPENDIX: ADDITIONAL RESULTS

Hover flight, comparison of the flow fields for the 4-rotors configurations, and vertical velocity contours on a $X-Z$ vertical plane passing though the rotors centerline. Hover flight, comparison of the flow fields for the 8-rotors configurations, and vertical velocity contours on a vertical plane passing through the rotors hub centerline. Climb flight, comparison of

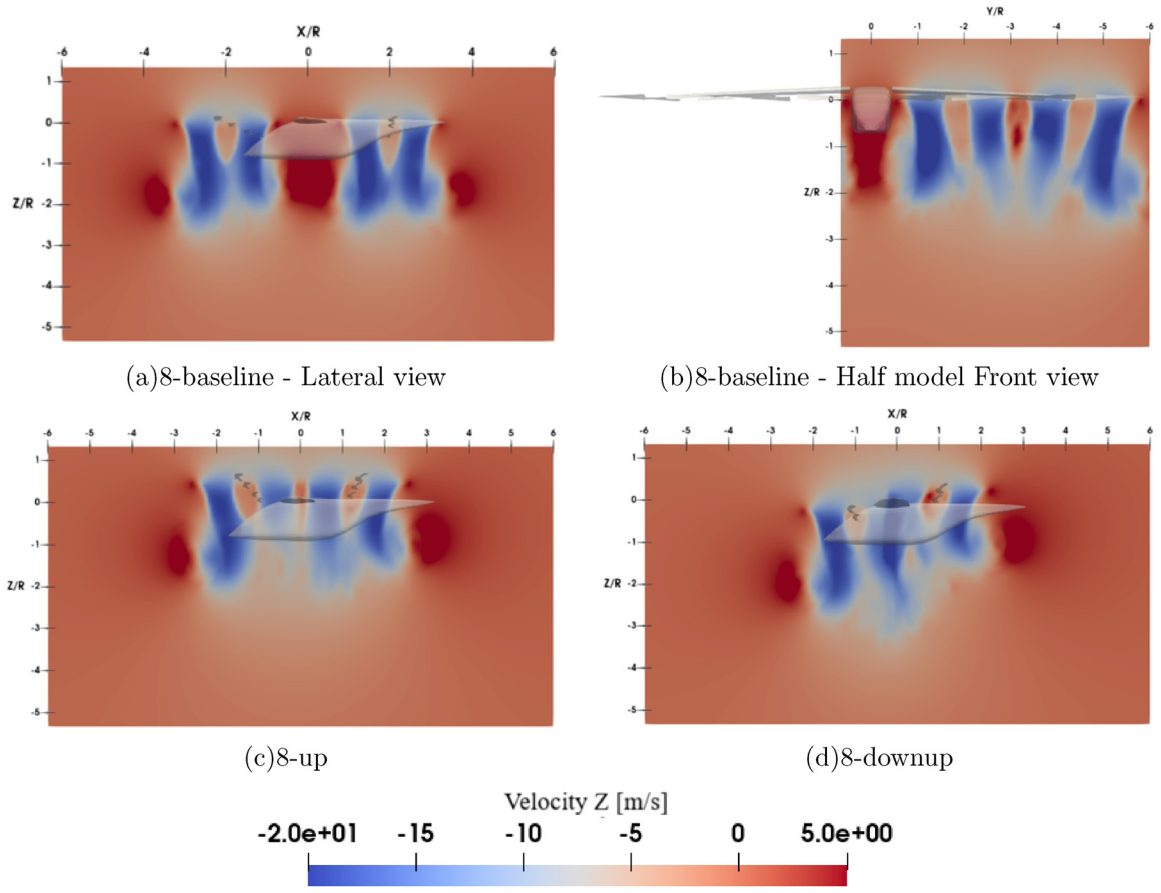

FIG. 22. Hover flight, comparison of the flow fields for the 8-rotors configurations, and vertical velocity contours on a vertical plane passing through the rotors hub centerline.

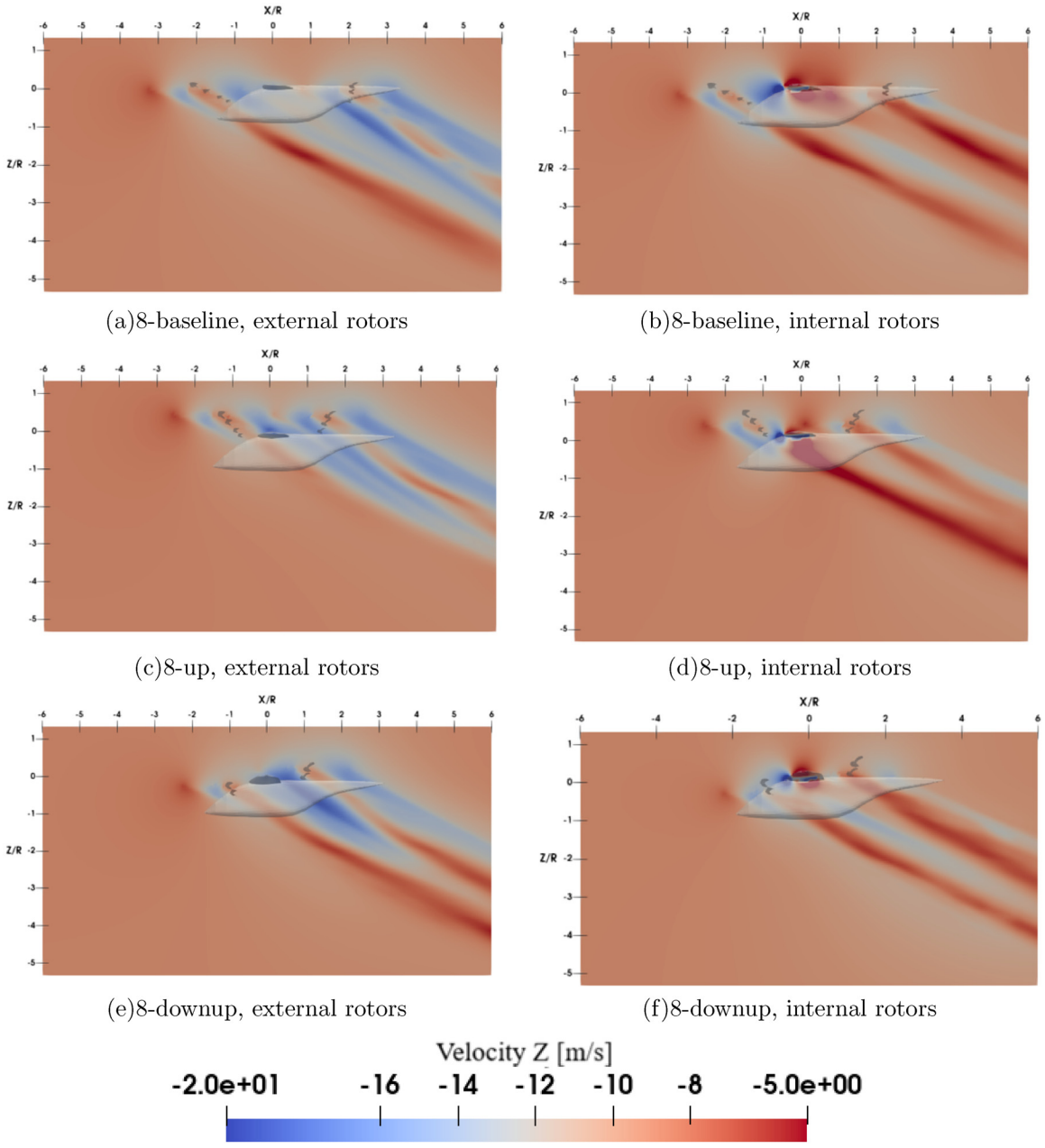

FIG. 23. Climb flight, comparison of the flow fields for the 8-rotors configurations, and vertical velocity contours on a $X - Z$ vertical plane passing through the rotors hub centerline.

the flow fields for the 8-rotors configurations, and vertical velocity contours on a $X - Z$ vertical plane passing through the rotors hub centerline.

REFERENCES

[1]P. Yedavalli and J. Mooberry, *An Assessment of Public Perception of Urban Air Mobility (UAM)* (Airbus UTM: Defining Future Skies, 2019).
[2]W. Johnson and C. Silva, "NASA concept vehicles and the engineering of advanced air mobility aircraft," Aeronaut. J. **126**, 59–91 (2022).
[3]A. Zanotti and D. Algarotti, "Aerodynamic interaction between tandem overlapping propellers in eVTOL airplane mode flight condition," Aerosp. Sci. Technol. **124**, 107518 (2022).
[4]G. Altamirano, J. Matt, S. Farrell, and A. Palazzo, "Static and forced oscillation wind tunnel tests of a tandem propeller configuration," in AIAA SCITECH 2025 Forum, AIAA Paper No. 2025-0664, 2025.
[5]R. Piccinini, M. Tugnoli, and A. Zanotti, "Numerical investigation of the rotor-rotoraerodynamic interaction for eVTOL aircraft configurations," Energies **13**, 5995 (2020).
[6]W. Zhou, Z. Ning, H. Li, and H. Hu, "An experimental investigation on rotor-to-rotor interactions of small UAV propellers," in Proceedings of the

35th AIAA Applied Aerodynamics Conference, Denver, CO, USA, 5–9 June 2017.
[7]D. Granata, A. Savino, D. Grassi, L. Riccobene, and A. Zanotti, "Aerodynamic and aeroacoustics investigation of tandem propellers in hover for eVTOL configurations," Aerosp. Sci. Technol. **155**, 109740 (2024).
[8]C. Poggi, G. Bernardini, M. Gennaretti, and R. Camussi, "Scalability of Mach number effects on noise emitted by side-by-side propellers," Appl. Sci. **12**, 9507 (2022).
[9]T. C. A. Stokkermans, D. Usai, T. Sinnige, and L. L. M. Veldhuis, "Aerodynamic interaction effects between propellers in typical eVTOL vehicle configurations," J. Aircr. **58**, 815 (2021).
[10]A. A. Kostek, J. N. Braukmann, F. Lößle, A. Visingardi, R. Boisard, and A. D. Gardner, "Influence of vertical rotor spacing on aerodynamic efficiency of quadcopter configurations," CEAS Aeronaut. J. **2025**, 1869–5590.
[11]T. Sinnige, N. van Arnhem, T. C. A. Stokkermans, G. Eitelberg, and L. L. M. Veldhuis, "Wingtip-mounted propellers: Aerodynamic analysis of interaction effects and comparison with conventional layout," J. Aircr. **56**, 295–312 (2019).
[12]A. Zanotti, L. Menini, A. Savino, D. Grassi, and L. Riccobene, "Experimental investigation of wing-propeller aerodynamic interaction in eVTOL configurations," Aerosp. Sci. Technol. **152**, 109348 (2024).
[13]J. A. Cole, T. Krebs, D. Barcelos, and G. Bramesfeld, "Influence of propeller location, diameter, and rotation direction on aerodynamic efficiency," J. Aircr. **58**, 63–71 (2021).
[14]M. Schollenberger, T. Lutz, D. P. Bergmann, and A. Strohmayer, "Numerical investigation of the influence of geometric and operational parameters on the aerodynamic interactions of wingtip mounted propellers," in *AIAA AVIATION 2022 Forum* (American Institute of Aeronautics and Astronautics, 2022).
[15]A. Bacchini, E. Cestino, B. Van Magill, and D. Verstraete, "Impact of lift propeller drag on the performance of eVTOL lift+cruise aircraft," Aerosp. Sci. Technol. **109**, 106429 (2021).
[16]O. Westcott, R. Entwistle, S. Krishna, and C. Paruchuri, "Aeroacoustics of lift + cruise eVTOL configurations during transition," in *AIAA Aviation Forum and Ascend 2025* (AIAA, 2025).
[17]K. Marepally, J. Baeder, Z. Habana, J. Goericke, and R. Plumley, "Aerodynamic analysis of stopped and stopping rotors in lift+cruise eVTOL configurations," in Vertical Flight Society 81st Annual Forum and Technology Display, 2025.
[18]Y. Liu, C. T. Druyor, and L. Wang, "High-fidelity analysis of lift+cruise VTOL urban air mobility concept aircraft," in AIAA AVIATION Forum, San Diego, CA, USA, 12–16 June 2023.
[19]E. J. Alvarez and A. Ning, "Modeling multirotor aerodynamic interactions through the vortex particle method," in AIAA Aviation 2019 Forum, AIAA Paper No. 2019-2827, 2019.
[20]M. Tugnoli, D. Montagnani, M. Syal, G. Droandi, and A. Zanotti, "Mid-fidelity approach to aerodynamic simulations of unconventional vtol aircraft configurations," Aerosp. Sci. Technol. **115**, 106804 (2021).
[21]A. Zanotti, A. Velo, C. Pepe, A. Savino, D. Grassi, and L. Riccobene, "Aerodynamic interaction between tandem propellers in evtol transition flight configurations," Aerosp. Sci. Technol. **147**, 109017 (2024).
[22]C. Niro, A. Savino, A. Cocco, and A. Zanotti, "Mid-fidelity numerical approach for the investigation of wing-propeller aerodynamic interaction," Aerosp. Sci. Technol. **146**, 108950 (2024).
[23]A. Savino and A. Zanotti, "Aerodynamic interaction between wing and propeller in eVTOL airplane mode flight condition," CEAS Aeronaut. J. (2025).
[24]G. Droandi, M. Syal, and G. Bower, "Analysis of the interactional aerodynamics of the Vahana eVTOL using a medium fidelity open source tool," in *Proceedings of the VFS Aeromechanics for Advanced Vertical Flight Technical Meeting* (AHS International, San Jose, CA, USA, 2020).
[25]G. Bucherelli, L. Das, D. Granata, and A. Zanotti, "Mid-fidelity numerical investigation of the interactional aerodynamic mechanisms in an electrical vertical take-off and landing quad-rotor aircraft," Phys. Fluids **37**, 067138 (2025).
[26]S. Wang, C. Kangni, Y. Safadi, and O. Pedretti, see https://www.dicua-m2026.org/common-uam-model for "Dicuam" (2026).
[27]G. H. Cottet, *Vortex Methods: Theory and Practice* (Cambridge University Press, 2000).
[28]G. S. Winckelmans, "Topics in vortex methods for the computation of three- and two-dimensional incompressible unsteady flows," Ph.D. thesis (California Institute of Technology, 1989).
[29]K. Lindsay and R. Krasny, "A particle method and adaptive treecode for vortex sheet motion in three-dimensional flow," J. Comput. Phys. **172**, 879–907 (2001).
[30]R. E. Brown and A. J. Line, "Efficient high-resolution wake modeling using the vorticity transport equation," AIAA J. **43**, 1434–1443 (2005).
[31]M. Tugnoli, D. Montagnani, A. Savino, A. Cocco, A. Colli, and A. Zanotti, (2025). "Dust Theory Manual," Zenodo. https://doi.org/10.5281/zenodo.17347327
[32]J. Yin, F. De Gregorio, K. Rossignol, L. Rottmann, G. Ceglia, G. Reboul, G. Barakos, G. Qiao, M. Muth, M. Kessler *et al.*, "Acoustic and aerodynamic evaluation of DLR small-scale rotor configurations within Garteur AG26," in Proceedings of the 49th European Rotorcraft Forum, Bückeburg, Germany, 5–7 September 2023.
[33]C. Leonard and B. Litherland, see https://sacd.larc.nasa.gov/uam-refs/ for "NASA UAM Reference Vehicles" (2024).
[34]C. Silva, W. Johnson, E. Solis, M. D. Patterson, and K. R. Antcliff, "VTOL urban air mobility concept vehicles for technology development," in *Proceedings of the AIAA Aviation Technology, Integration, and Operations Conference* (AIAA, Atlanta, GA, USA, 2018).
[35]L. Abergo, F. Caccia, A. Zanella, M. Ubezio, and A. Guardone, "Tonal noise emission of an elastic propeller in hover using a mid-fidelity approach," in AIAA SCITECH 2025 Forum, AIAA Paper No. 2025-1241, 2025.
[36]A. Zanotti, A. Savino, M. Palazzi, M. Tugnoli, and V. Muscarello, "Assessment of a mid-fidelity numerical approach for the investigation of tiltrotor aerodynamics," Appl. Sci. **11**, 3385 (2021).
[37]A. Zanotti, "Experimental study of the aerodynamic interaction between side-by-side propellers in eVTOL airplane mode through stereoscopic particle image velocimetry," Aerospace **8**, 239 (2021).
[38]B. Ortun, R. Boisard, and I. Gonzalez-Martino, "In-plane airloads of a propeller with inflow angle: Prediction vs. experiment," in 30th AIAA Applied Aerodynamics Conference, AIAA Paper No. 2012-2778, 2012.